MICROSTRUCTURE AND MECHANICAL PROPERTIES OF FRICTION STIR WELDED ALUMINUM ALLOY AL6061-T651

A Thesis Submitted to the College of
Graduate and Postdoctoral Studies
In Partial Fulfillment of the Requirements
For the Degree of Master of Science
In the Department of Mechanical Engineering
University of Saskatchewan
Saskatoon

By
Vidit Yogeshkumar Patel

© Copyright Vidit Yogeshkumar Patel, July 2020. All rights reserved.

PERMISSION TO USE

In presenting this thesis in partial fulfillment of the requirements for a Postgraduate degree from the University of Saskatchewan, I agree that the Libraries of this University may make it freely available for inspection. I further agree that permission for copying of this thesis in any manner, in whole or in part, for scholarly purposes may be granted by Prof. Jerzy Szpunar, who supervised my thesis work or, in their absence, by the Head of the Department or the Dean of the College in which my thesis work was done. It is understood that any copying or publication or use of this thesis/dissertation or parts thereof for financial gain shall not be allowed without my written permission. It is also understood that due recognition shall be given to me and to the University of Saskatchewan in any scholarly use, which may be made of any material in my thesis.

Requests for permission to copy or to make other uses of materials in this thesis/dissertation in whole or part should be addressed to:

Head of the Department of Mechanical Engineering
University of Saskatchewan
57 Campus Drive
Saskatoon, Saskatchewan S7N 5A9 Canada

OR

Dean
College of Graduate and Postdoctoral Studies
University of Saskatchewan
116 Thorvaldson Building, 110 Science Place
Saskatoon, Saskatchewan S7N 5C9 Canada

ABSTRACT

Since the beginning of the 21st century and rapid developments in various industries, the demand for strong, light weight, and robust materials that can be used in extreme environments has increased. The use of such materials has been significant in the transportation sector, where reduction in fuel consumption and emission of harmful gases are required. Aluminum is one of the most suitable metals that can be alloyed with different elements to obtain desired properties. However, joining of aluminum using conventional welding processes for special applications in aerospace, shipbuilding, and automobile industries has been a challenge. Friction stir welding (FSW) is a widely used method to weld aluminum since its invention because it overcomes most of the challenges related to aluminum welding. The objective of this research was to analyze the role of preheating and post-cooling applied before and after FSW on the microstructure and some mechanical properties of Aluminum alloy Al6061-T651.

Various characterization techniques such as optical microscopy (OM), scanning electron microscopy (SEM), and electron backscattered diffraction have been used to examine the weldment of Al 6061- T651 plates. Analysis of different weld zones formed after the process such as nugget zone (NZ), thermomechanically affected zone (TMAZ), heat affected zone (HAZ) along with the parent metal or base metal (PM or BM) showed equiaxed and recrystallized grains in NZ, deformed and partially recrystallized grains in TMAZ and overaged grains in HAZ. 10% decrease and a 3% increase in the average hardness of NZ was seen in preheated and post-cooled samples, respectively. Hardness was lowest in the HAZ, a bit higher in TMAZ and NZ and highest in PM. Moreover, it was concluded that hardness is not dependent on the grain size to a large extent. SEM of the fractured samples revealed that the mode of failure is ductile and took place in the HAZ. The tensile test results showed only less than 5% and 1% change in tensile strength and percent of elongation of the welded samples, respectively. Overall, it was found that the peak temperature and the duration of the heat cycle have a higher impact on the microstructure and mechanical properties compared to the plastic deformation.

ACKNOWLEDGMENT

I would like to express my deepest gratitude to my supervisor Prof. Jerzy Szpunar for providing me with the opportunity to carry out my M.Sc. program under his guidance. This research would not have been possible without his leadership, encouragement, and scientific contributions. My sincere thanks to Dr. Vishvesh Badheka (Pandit Deendayal Petroleum University) for providing me with samples, his insightful guidance in the time of need, and setting up a platform for me to come to University of Saskatchewan and carry out the further research.

I would also like to acknowledge the Department of Mechanical Engineering for its support throughout my masters. To Mr. Nan Fang Zhao for his training for using various lab equipment. I would like to thank my advisory committee members Prof. Ike Ogoucha and Prof. Mohamed Boulifiza, for their valuable suggestions and support in my research project.

I appreciate the support of all my colleagues from the Advanced Materials and Renewable Energy Lab (Dr. Salman, Linu, Tiamyu, Ketan, Joseph, Mustafijur Rahman, Xu, Mohsen, Omar, Ubong and Alen) for their help and co-operation. Also, many thanks to my friends who became a family and the people who supported me mentally and financially in times of need.

Lastly, my heartful thanks to my father (Mr. Yogehskumar Patel) for mentally supporting me and my mother (Mrs. Bhagwati Patel) for being a constant source of inspiration. A huge thanks to my brother (Mr. Smit Patel) for reminding me to take breaks from work and enjoy life some times. Also, many thanks to my fiancée (Miss Avani Golakia) for believing in me.

DEDICATION

I dedicate this thesis to my beloved parents, Mr. Yogeshkumar Dahyabhai Patel and Mrs. Bhagwati Yogeshkumar Patel, and my brother Mr. Smit Yogeshkumar Patel, and my fiancée Miss Avani Golakia; for their unconditional love and support.

TABLE OF CONTENTS

LIST OF TABLES

LIST OF FIGURES

LIST OF ABBREVIATIONS

FSW	Friction Stir Welding
NZ	Nugget zone
TMAZ	Thermomechanically affected zone
HAZ	Heat affected zone
PM	Parent metal
KM	Kernel misorientation
REX	Recrystallized fraction
GTAW	Gas tungsten arc welding
GMAW	Gas metal arc welding
EBSD	Electron backscattered diffraction
OM	Optical microscopy
SEM	Scanning electron microscopy
LAGB	Low angle grain boundaries
HAGB	High angle grain boundaries
VHN	Vickers hardness number
TEM	Tunneling electron microscopy
DSC	Differential scanning calorimetry
PWHT	Post weld heat treatment
PAW	Plasma arc welding
EBW	Electron beam welding
LBW	Laser beam welding
TIG	Tungsten inert gas
MIG	Metal inert gas
AA	Aluminum Association

INTRODUCTION

1.1 Background

Aluminum is the third most abundant element in the earth's crust and the most abundant metallic element. For the last 50 years, it has been second only to iron in its industrial use" [1]. Out of the 1 billion tons of aluminum produced to date, almost 75% of it is still in use [2]. Being lightweight, corrosion-resistant, durable, ductile, versatile, and highly recyclable, it has found applications in a variety of industries like building and construction, electrical, electronics, and appliances, foil, and packaging. Various alloying metals can be added to pure Al and based on the applications; desired mechanical properties can be obtained. With the demand for fuel-efficient transportation methods, while maintaining strength and safety, automakers, aircraft companies, and aerospace industries are turning to aluminum [3]. One of the biggest challenges in using aluminum alloys for such applications is the joining of these alloys using conventional welding processes, as the required quality and mechanical properties of joints must be high. Preheating and higher heat input may be necessary while welding aluminum, which results in more substantial deformation as it has much higher thermal conductivity, higher heat capacity, and more thermal expansion than steel. Moreover, aluminum forms an oxide layer on the surface when exposed to air, which interferes with the merger of the joint. The melting point of the oxide layer is 2000 °C, whereas that of aluminum is 660 °C and so the oxide does not dissolve in the weld bath and needs to be destroyed locally [4].

1.2 Overview of Friction Stir Welding

Friction stir welding is a solid-state joining process that was invented at The Welding Institute (TWI) in the UK in 1991 [5]. A non-consumable rotating tool with a profiled pin and shoulder is plunged into the interface of two workpieces and moved in the direction of the joint. The localized heating around the pin softens the material, and the mixing of material takes place because of the rotational and translational motion of the tool. The tool shoulder helps retain the heat produced and prevents upward displacement of the workpieces. Heat efficiency of the FSW process is 95%,

compared to 60 to 80% in the fusion welding processes. Only 5% of the total heat generated flows through the tool [6]. A schematic drawing of friction stir welding is shown in Figure 0.1. Fine equiaxed recrystallized grains are formed because of intense plastic deformation in NZ, which results in better mechanical properties [7]–[10].

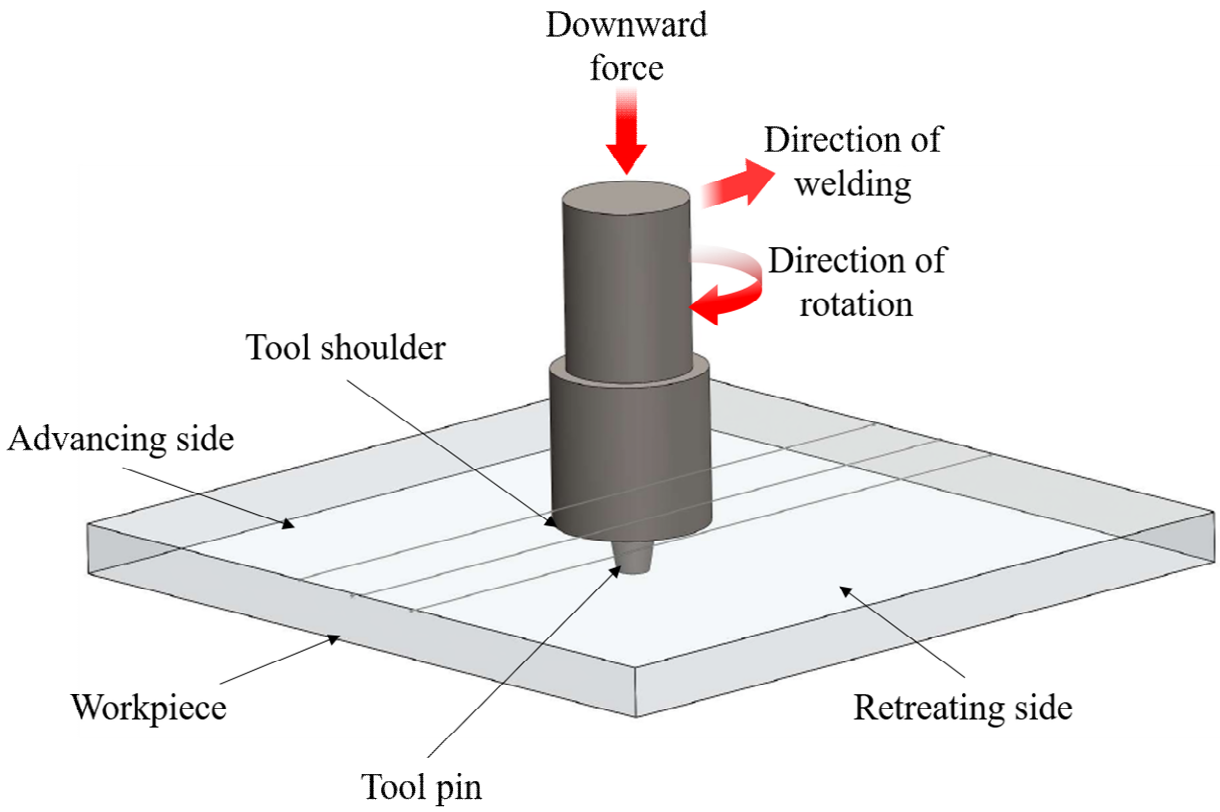

Figure 0.1. Schematic drawing of friction stir welding.

Cost of the general process [11]:

The FSW process has both positive and negative sides in terms of the cost depending on the applications. Plates with higher thickness can be weld in a single pass with the FSW process. In contrast, multiple passes with inter pass cooling, cleaning, repair, and rotation of workpiece are necessary after every pass during arc welding processes. This reduces the processing time leading to a significant reduction in labor costs. On the other side, the licensing fee of the FSW process is higher as the TWI is the owner of the intellectual property rights, which leads to an increase in the overall cost of the process and can be impractical for certain smaller applications. The FSW

process is highly mechanized and requires the welding setup with expensive tools; higher tool rotation speeds with transverse motion along the joint, and different fixtures to hold the workpiece during the welding, eventually leading to higher capital investment compared to the conventional welding processes.

Moreover, based on the volume of production, it can be practical or impractical compared to the arc welding processes. Sometimes, the lack of skilled workforce for arc welding processes, savings from labor and processing times, and other costs, including licensing and capital investment, can overall make FSW a more economical option compared to the arc welding processes. Certain factors like the cost of shielding gases and filler metal and reduced energy consumption result in an overall reduction in the cost of the whole process.

Compared to conventional arc welding processes, FSW has several advantages, as mentioned below:

- Environmental benefits: no flux or shielding gas required, no surface cleaning or edge preparation required, no fumes, or spatter.
- Energy benefits: only 2.5% of the energy that is required for laser welding is used.
- Structural benefits: no hot cracking, porosity or solidification cracking, less shrinkage, and distortion, excellent repeatability, no filler metal required, better mechanical properties.

Some of the disadvantages of FSW are mentioned below:

- Less flexible compared to manual and arc welding processes.
- Exit hole when the tool is withdrawn from the workpieces leads to wastage of material.
- Cannot be used for making joining huge parts of various machines because of the limitations of the welding setup and fixtures.
- Requires strong jigs and fixtures as the downward and transverse forces are high during the process [12], [13].

1.3 Applications of FSW

Apart from aluminum alloys, FSW can be used to join magnesium, copper, hafnium, zirconium, Inconel, titanium, superalloys, steel and ferrous alloys, and other dissimilar metals which are difficult to join using conventional arc welding processes [14]. NASA has been using FSW since the 2000s in manufacturing external tanks for space shuttles, the Space Launch System Core Stage, and various other parts [15]. Eclipse Aviation was able to replace almost 7000 rivets by using friction stir welds instead, in the production of its Eclipse 500 business jet [16]. The Boeing Company reported 60% cost saving and reduced the manufacturing time to 6 days from 23 for the Delta IV and Delta II [17]. Some of the well-known automobile companies like Volvo, Chrysler, Rover, Tower Automotive, Ford, General Motors, BMW are sponsoring a confidential project to incorporate FSW in their production lines [18]. The use of FSW to weld aluminum alloy Def Stan 95-22 Class 1 instead of MIG by the Ministry of Defense in the UK, has shown better exfoliation corrosion and stress corrosion resistance [19]. In the US, Advanced Amphibious Assault Vehicle (AAAV) manufactured using 5083Al-H131 was welded using FSW, resulting in a 300% increase in ductility and an increase of 124MPa tensile strength compared to when welded using GMAW [20], [21].

1.4 Research Objectives

In the present study, the changes in microstructure and mechanical properties of friction stir welded Al 6061 are studied. The specific objectives are as follows:

1. To evaluate the microstructure of FSWed samples with preheating and post-cooling.
2. To determine the effect of preheating and post-cooling on the hardness of welded samples.

1.5 Thesis Arrangement

This thesis consists of five chapters. Chapter one gives an overview of aluminum and friction stir welding of Al alloys. The second chapter discusses the welding of aluminum using conventional welding processes, imperfections due to those processes, the reason for friction stir welding, and background of research carried out related to this study in some details. Material, tools, equipment,

and the methods used in this study are mentioned in the third chapter. The outcomes in the form of results and discussion are presented in the fourth chapter. The fifth and final chapter of the thesis gives an overall conclusion from the present study and also outlines recommendations for future work.

LITERATURE REVIEW

1.6 Aluminum Alloys

About 80% of the total use of aluminum is for wrought products like plates, sheets, extrusions, and wire [22]. Wrought alloys are then subdivided heat treatable and non-heat-treatable alloys. According to the classification by American National Standards Institute (ANSI) standard H35.1, 1000 (pure Al), 3000, 4000, and 5000 series alloys are non-heat-treatable. It means that their strength can be improved using cold-working or work hardening. Whereas 2000, 6000 and 7000 series alloys are heat treatable alloys, which can be strengthened by different heat treatments. Based on their applications pure aluminum is alloyed with specific elements is defined proportions, for example, 3000 series alloys consist of Mn which offers excellent formability, 4000 series alloys consist of Si for higher temperature applications, Mg is added to aluminum to make 5000 series alloy for excellent corrosion resistance, to obtain high strength Cu is added to manufacture 2000 series alloys, Mg and Si when added offer good weldability and higher corrosion resistance in 6000 series alloys and aluminum is alloyed with Zn to form 7000 series alloys for applications where higher strength to weight ratio is necessary [22], [23].

Aluminum 6061 is an alloy consisting of aluminum with Mg and Si as main alloying elements with traces of other elements like Cr, Mn, Ti, and others. It is considered as one of the most versatile aluminum alloys because of its superior corrosion resistance, good formability, and weldability. It gains its strength from the Mg_2Si precipitates. To increase the strength of the alloy, it is solution-treated within the solid solution limit of the alloying element and kept at the same elevated temperature until the solute particles dissolve. It is then quenched to room temperature, and then the solution is again heated to a specific temperature where it is kept for a fixed time so that stable precipitates are formed and then it is cooled to room temperature [24].

1.7 General welding techniques used to join aluminum

Welding processes mainly used to weld aluminum are arc welding processes like GMAW/MIG welding(gas metal arc welding/metal inert gas), GTAW/TIG welding (gas tungsten arc welding/tungsten inert gas), PAW (plasma arc welding), beam welding processes like LBW (laser beam welding) and solid-state welding processes like FW (friction welding) and FSW. Out of the processes mentioned above, GMAW and GTAW are the most widely used to join aluminum. GTAW is used to weld plates of up to 3 mm thickness, whereas GMAW is used to join thicker plates. Laser beam welding is mainly used in the automobile industry, where highly mechanized welds are made using automatic welding robots. Meanwhile, solid-state processes are mostly used to join dissimilar alloys and alloys, which are difficult to join using the conventional welding processes and need higher mechanical properties for particular applications.

1.8 Imperfections due to conventional welding processes

Mentioned below are some of the main imperfections resulting in lower weld quality in Al alloys when welded using arc welding processes:

1. Solidification cracking: Al alloys, especially 2xxx, 6xxx, and 7xxx series, are sensitive to solidification cracking. It is mainly due to high stresses generated as a result of higher thermal expansion (almost twice that of steel) during welding and higher contraction during solidification of the weld pool (almost 5% than that in steel). Besides solidification cracking, liquation cracking (in HAZ) and cracking due to alloy segregation (in fusion/nugget zone) might also take place while using conventional welding processes to weld aluminum [4], [25].
2. Porosity: Liquid aluminum has a tendency of absorbing hydrogen, but during solidification, solubility factor decreases by a factor of 20, resulting in the formation of hydrogen bubbles or pores. The primary sources of hydrogen are moisture, contaminants on the workpiece, shielding gases, or the surrounding atmosphere [25].
3. Inclusions: During TIG welding, tungsten may be transferred through the arc, which results in metallic inclusions in the weld. Apart from that, oxygen and nitrogen can form oxides and nitrides with aluminum, which deteriorates mechanical properties [4].

1.9 Conventional welding processes vs FSW

Conventional welding processes such as GTAW, GMAW, or electron beam welding (EBW), resulting in the formation of coarse, semi-cast grain structure in the fusion zone, partially-melted zone, and the heat-affected zone [26]. On welding AA2219 by FSW, GTAW, and EBW, joint efficiency (equation 2.1) of 72% (20% higher than that of GTAW and 12% higher than that of EBW) was obtained by FSW. Also, the fatigue strength obtained by FSW was 60% higher than that of GTAW and 20% higher than that of EBW joints. Meanwhile, pitting corrosion resistance was reported to be the lowest in FSWed samples [27]. The main reason for higher tensile and fatigue strength and lowest corrosion resistance is the formation of equiaxed grains, uniformly distributed strengthening precipitates, and higher dislocation density in the NZ [27], [28]. When AA2023-T3 alloy was welded using TIG, it leads to severe distortion and high tensile residual stresses, and it was not possible to obtain untensioned welds even after using mechanical tensioning. In contrast, when the same alloy was welded using FSW, it showed high distortion, but on mechanical tensioning, untensioned welds could be obtained [29].

$$\text{Joint efficiency} = \frac{\text{Tensile strength of the weld}}{\text{Tensile strength of the base metal}} \times 100 \qquad (0.1)$$

1.10 Effects of various welding variables during friction stir welding

Compared to the conventional arc welding processes, friction stir welding has fewer variables that affect the microstructure and the mechanical properties of the workpiece. Mainly during any welding process, the changes in the welding parameters result in a change in the peak temperature and the duration of the thermal cycle. Some of the main parameters in the FSW process and their respective effects on the peak temperature and thermal cycles are discussed below:

1. Tool design: The main functions of the shoulder of the rotating tool in friction stir welding are to generate the heat and to prevent the material from escaping the workpiece, and that of the pin is to uniformly distribute the materials on advancing and retreating sides of the workpiece. In this way, tool design becomes an essential factor in influencing heat generation, plastic flow,

and the uniformity of the welded joint [30]. On using column and taper tools for the FSW process, Zhao et al. [31] found a hole defect in the NZ, but when a taper tool with screw threads was used, there was improved vertical material flow, and no hole defect was observed. The tapered tool with the thread also generated more heat. After much research, the TWI has designed various tool designs, as mentioned below [32]–[36]:

- Whorl tool- tapered threads help create a vertical component of velocity, which improves plastic flow.
- MX-Triflute- the flute helps increase the surface area between the workpiece and the tool generating more heat and hence leading to the softening of material and better flow.
- Flared-Triflute- similar to MX-Triflute but with an expanded flute.
- A-skew- a tapered threaded tool with an inclined axis. Flared-Triflute and A-skew tools help in performing lap joints by increasing the swept volume relative to the pin leading to a broader weld region.
- Re-stir- helps in symmetric material flow by applying periodic reversal of the tool rotation.

2. Tool dimensions: Liu et al. [37] reported that the shape of the NZ changed from rectangular to elliptical, and the inclination of the HAZ to the butting surfaces increased when the tool diameter was changed from 16 mm to 24 mm keeping other welding parameters constant. Moreover, it was observed that the position and inclination of the HAZ changed when shoulder and pin dimensions were changed without any impact on the hardness across the weldment. However, no significant change in the heating and cooling rates was observed when the tool dimensions were changed.

3. Welding speed (mm/min): Liu et al. [38] reported that hardness and tensile strength increased when the welding speed was increased from 200 to 600 mm/min keeping other parameters constant. Also, it was noticed that the duration of thermal cycles at higher temperatures reduced with higher welding speed, eventually leading to lower heat input compared to other conditions [37]. An increase in welding speed slightly reduces the peak temperature and also decreases the nugget size, but after a specific limit, it becomes constant [38].

4. Tool rotation rate (rpm): When Kwon et al. [39] increased the tool rotation speed from 560 to 1840 rpm, a linear increase in temperature from 190 to 360 ° was reported. Also, at higher tool rotation speeds, the rise in peak temperature became gradual. Similarly, Tang et al. [40] reported an increase in temperature by increasing the tool rotation and weld pressure. The nugget size also increases with the increase in tool rotation speed. Grain size increases with an increase in tool rotation speed, and after a limit, the increase of grain size becomes slower. Yield strength increases with an increase in rotation speed. Also, higher rotation speeds result in higher ductility in the welds. However, excessive tool rotation rate leads to lower torque and hence lower peak temperature leading to lower ductility [38].

5. Axial pressure: Nandan et al. [30] observed that an increase in axial pressure increases peak temperature but not drastically. In short, excessive axial pressure can lead to overheating and thinning of the joint, whereas lower axial pressure results in insufficient heating and pores/voids. It should also be kept in mind that an increase in axial pressure requires higher power for the operation.

6. Tilt angle (°): When welding polyethylene using FSW, Arici et al. reported a decrease in tensile strength with the increase in tool tilt angle. The thickness of the NZ reduces with higher tool tilt angles, and hence it reduces the tensile strength [41]. A group of researchers observed defects on the surface while using a 3° tool tilt angle, which was dismissed when the tool tilt angle was reduced to 1°. With a higher tool tilt angle, the material can easily escape from the bottom of the tool shoulder as there is a more significant gap between the tool and the workpiece. This results in the formation of surface defects. They also reported that at lower tool tilt angles are equally undesirable to produce defect-free welds as the forging of material, essential for the weld, does not happen, and hence welding does not take place [42].

1.11 Preheating, post cooling or post-weld heat treatment of FSWed samples

The welding processes create different zones in the workpiece with varying microstructure depending on the peak temperature during the process and the thermal cycle due to welding. Similarly, after FSW, the workpiece can be divided into NZ, TMAZ, HAZ, and PM. Based on the

distance from the center of the weld, the NZ and the TMAZ undergo plastic deformation as well as the heat cycle, whereas the HAZ is only exposed to the heat cycle resulting from the welding process. Sato et al. [43] reported that the dissolution of precipitates takes place in the weld center, and the amount of dissolution decreases with an increase in distance from the center. Similarly, the coarsening of precipitates from PM to TMAZ, along with increasing dissolution and reprecipitation towards the NZ, was reported by Su et al. [44]. During the tensile tests on FSWed samples, it was seen that the samples mostly fractured from the HAZ of the retreating side of the weld because the tensile strain gets localized in this region [45]. Because of the above reasons, the HAZ becomes the region with the lowest hardness and hence the weakest region in the workpiece. To improve the properties of the HAZ and the overall weld, researchers have started using preheating, post-cooling, and post-weld heat treatments [46]–[51].

Tanaka et al. welded mild steel with aluminum alloy and concluded that no weld failed in the aluminum base metal and on comparing the joint strength of FSWed Al 7075-T6 to the interface strength of aluminum and mild steel, the interface strength was found out to be lower [52]. Because of this, researchers started using preheating using laser and reported that there were no intermetallic phases between steel and aluminum, resulting in high tensile strength of about 80% of the tensile strength of the aluminum alloy [53]. Bang et al. [51] FSWed Al 6061-T6 and STS 304 stainless steel assisted with TIG torch preheating and obtained transverse tensile strength of approximately 93% of the tensile strength of Al 6061 base metal resulting because of the higher plastic flow and partial annealing effect mainly in the steel which is desirable in dissimilar welds. Preheating the dissimilar welds also resulted in a significant increase in the elongation of welds.

Preheating the workpiece before welding has advantages as stated below [54]:

- It helps to increase the ductility of the workpiece by slowing down the cooling rate after welding and also improves the notch toughness of the overall weld.
- It reduces distortion and shrinkage stresses in different weld zones for alloys having a higher coefficient of thermal expansion.
- It also helps in reducing the wear and tear of the tool during the FSW process.
- Hydrogen trapping susceptibility and hot cracking chances reduce significantly when a workpiece is heated before welding.

When alloys with a higher melting point or higher conductivity are preheated before FSW, material flow is facilitated, and also the process window increases, resulting in sound welds. Reduction in extensive growth of recrystallized grains and dissolution of strengthening precipitates can be achieved by cooling the samples of alloys with lower melting points [13]. On cooling the Al 6061-Titanium friction stir welded samples in water, it resulted in higher tensile strength compared to the samples cooled using CO_2 or air or heated using a GTAW torch before the welding. Preheating of samples resulted in intermetallic inclusions and coarse grains, leading to almost twice the hardness compared to the cooled samples. It was also seen that the samples cooled using CO_2 resulted in finer grains compared to the as-welded samples, and the preheated samples resulted in larger grains as the cooling rate was slower compared to other conditions. Excess heat from the preheating resulted in the formation of porosities and cracks in NZ but increased the ductility than other samples [49]. Kush et al.[55] reported a better surface finish when the Al-Cu samples were cooled using compressed air or water compared to oxide formation on the surface when they were preheated using TIG torch. Higher elongation values were observed in preheated samples with higher current compared to the cooled samples with compressed air or water. They also observed a minor improvement in tensile strength at lower preheating current, which deteriorated with increased current. The highest tensile strength was reported for samples cooled with water, whereas all the samples showed higher hardness values in the NZ compared to the as-welded sample.

Post weld heat treatment on FSWed Al 6061O samples resulted in very coarse grains in the NZ and uniform hardness across the weldment. The samples failed during root bend test because of the presence of precipitate free zones near to the grain boundaries and larger grains [47]. Reddy et al. [56] assessed the mechanical properties, microstructure, and the residual stress distribution of FSWed Al 6061 in as-welded, post-weld aged, and post-weld solution treated and aged conditions. Overall, the post-weld solution treatment and ageing resulted in higher hardness and tensile strength compared to as-welded or post-weld aged samples. The hardness values obtained from post-weld aged samples were similar to those of post-weld solution treated and aged samples, but there was not much improvement in the tensile strength due to the age hardening of the NZ and over ageing in the HAZ. Residual stress analysis showed that there are compressive residual

stresses in the NZ and PM, whereas in the HAZ, it changes to tensile residual stresses. Post weld ageing results in localized stresses in the HAZ, but the stress distribution is uniform throughout the weldment after post-weld solution treatment and ageing. Also, it was noticed that the residual stress distribution in the as-welded condition is always asymmetric with the highest values in the advancing side because of higher thermal gradients.

On comparing the effects of solution treatment, artificial ageing, and a combination of both, better tensile strength and hardness were achieved by artificial ageing treatment after FSW. There was no change in the grain size after any post welding heat treatment. Overall, during normal FSW dissolution of precipitates takes place, during the solution treatment as well precipitates dissolve. Limited reprecipitation is seen during solution treatment, and the ageing supersaturated solution begins to form strengthening precipitates that are coarse and are aggregated near grain boundaries. In contrast, artificial ageing results in fine precipitates distributed uniformly, giving better hardness and tensile properties compared to other conditions [57]. Venkateswaralu et al. [50] reported that post-weld ageing after FSW of Al 6061 underwater resulted in higher tensile strength of 288 MPa and joint efficiency of 89.97%. On the contrary to the above discussion, Aydin et al. [48] observed that post-weld heat treatment results in abnormal grain growth in the NZ, resulting in lower hardness compared to the base metal. After carrying out the T6 heat treatment on initial T4 tempered samples, an increase in hardness of TMAZ, HAZ, and BM & higher strength was observed but it was always less than the base metal properties.

EXPERIMENTAL WORK

1.12 Materials

6.5 mm thick plates of aluminum alloy AA 6061- T651 were used as the base metal for the present study. T6 denotes that the alloy was solution heat-treated and artificially aged, and Tx51 applies that “no further straightening” [58] was performed after stretching into a plate. The chemical composition of the base metal was obtained from ASM Handbook, which is listed in Table 0.1[58].

Table 0.1. Chemical composition of Al alloy 6061-T651.

Element	Al	Mg	Si	Cr	Mn	Ti	Cu	Zn	Fe	Others
Wt. (%)	Bal	0.80-1.20	0.40-0.80	0.04-0.35	0.15	0.15	0.15-0.40	0.25	0.70	0.15

Base metal plates, each of dimensions 100 mm x 50 mm x 6.5 mm (as shown in Figure 0.1) were friction stir welded on a vertical milling machine using a non-consumable tool which was made from M2 grade high-speed steel. Its chemical composition is summarized in Table 0.2 [59]. Tool geometry and dimensions are shown in Figure 0.2.

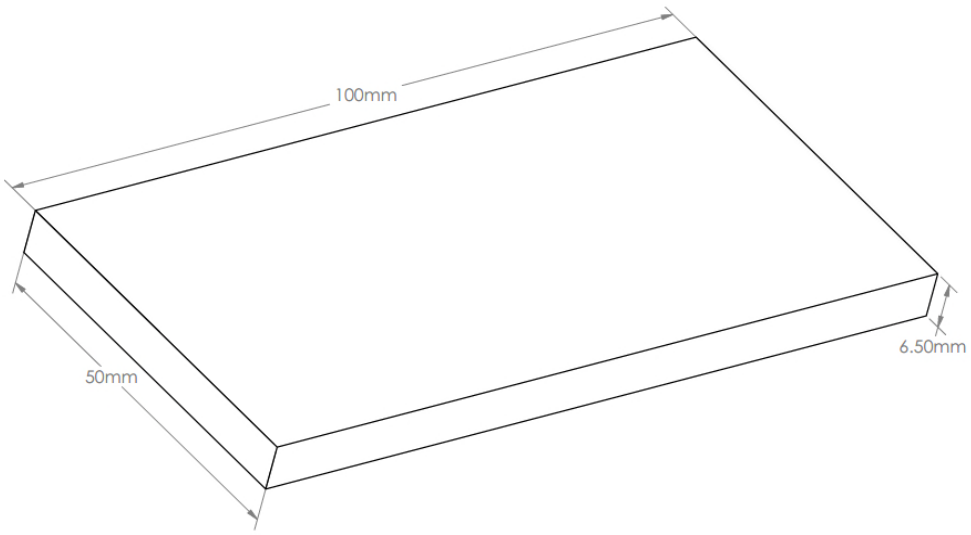

Figure 0.1. Sample plate with dimensions.

Table 0.2. Chemical composition of tool.

Element	Fe	C	Mn	Si	Cr	W	Ni	V	Cu	P	S
Wt. (%)	Bal	0.65-0.80	0.10-0..40	0.20-0.40	3.75-4.00	17.25-18.75	0.3	0.90-1.30	0.25	0.03	0.03

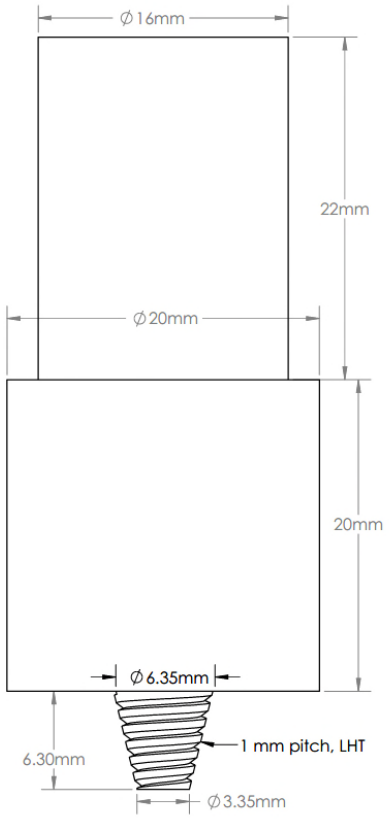

Figure 0.2. Friction stir welding tool with dimensions.

1.13 Welding Procedure

Friction stir welding was carried out on a vertical milling machine using tool rotation speed of 1500 rpm, welding speed of 50 mm/min, and tool tilt angle of 2° from the vertical axis. To prevent the displacement of plates and to retain the generated heat during the process, a fixture made out of 304-grade stainless steel was used. The model of the stainless steel fixture is shown in Figure 0.3.

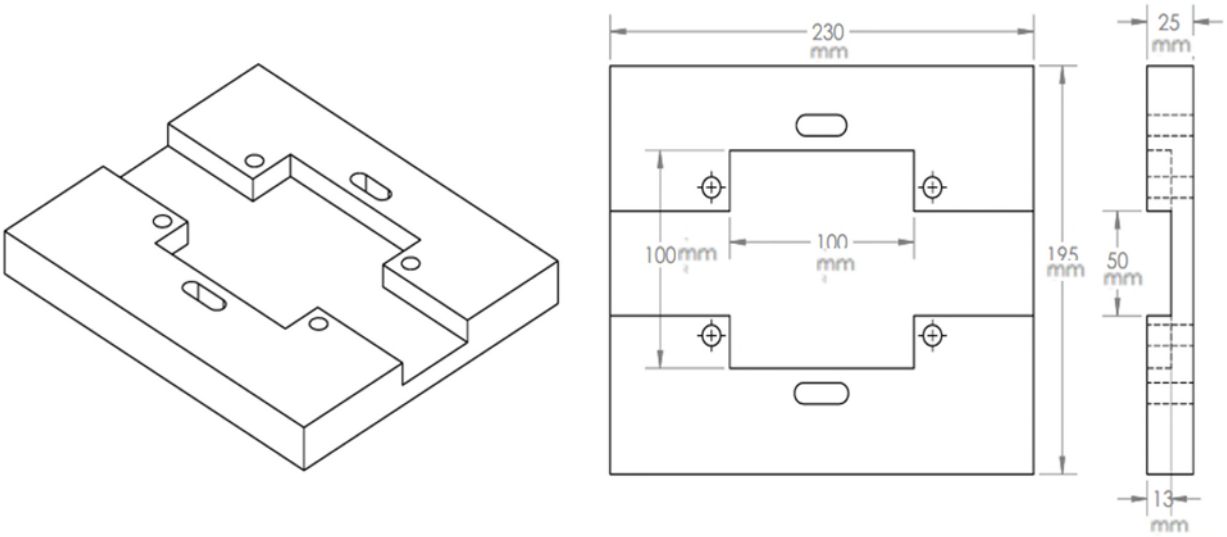

Figure 0.3. Model of stainless steel fixture with dimensions.

Welding was carried out in three different conditions: (1) Normal FSW, (2) FSW with preheating, and (3) FSW with post-cooling. Parameters of different conditions are mentioned in Table 0.3.

Table 0.3. Welding parameters.

Sr. No.	Condition	Parameters	Sample Description
1	Normal FSW	No preheating or post-cooling	FSW-0
2	Preheating (using GTAW torch)	10 A current	FSW-10A
3		20 A current	FSW-20A
4	Post-cooling (using compressed air)	10 psi pressure	FSW-10
5		20 psi pressure	FSW-20

Normal FSW: No preheating or post-cooling was applied for this trial.

Preheating using GTAW Torch: A GTAW torch (Model: Panasonic YC-200 BR1, 200 amperes, single-phase, AC/DC power source) was placed ahead of the FSW tool along the joint line.

Post-cooling using Compressed Air: After the FSW process, cold air coming out from a compressor (Model: Air Marshal. 200 psi, 5HP) was applied along the weld joint as a cooling source.

To measure temperature for the processes, a K-type thermocouple was attached to the samples during all the trials. The overall experimental setup is shown in Figure 0.4. The friction stir welding trials were conducted at Pandit Deendayal Petroleum University, Gandhinagar, India, with financial support from the Indian Space Research Organization (ISRO).

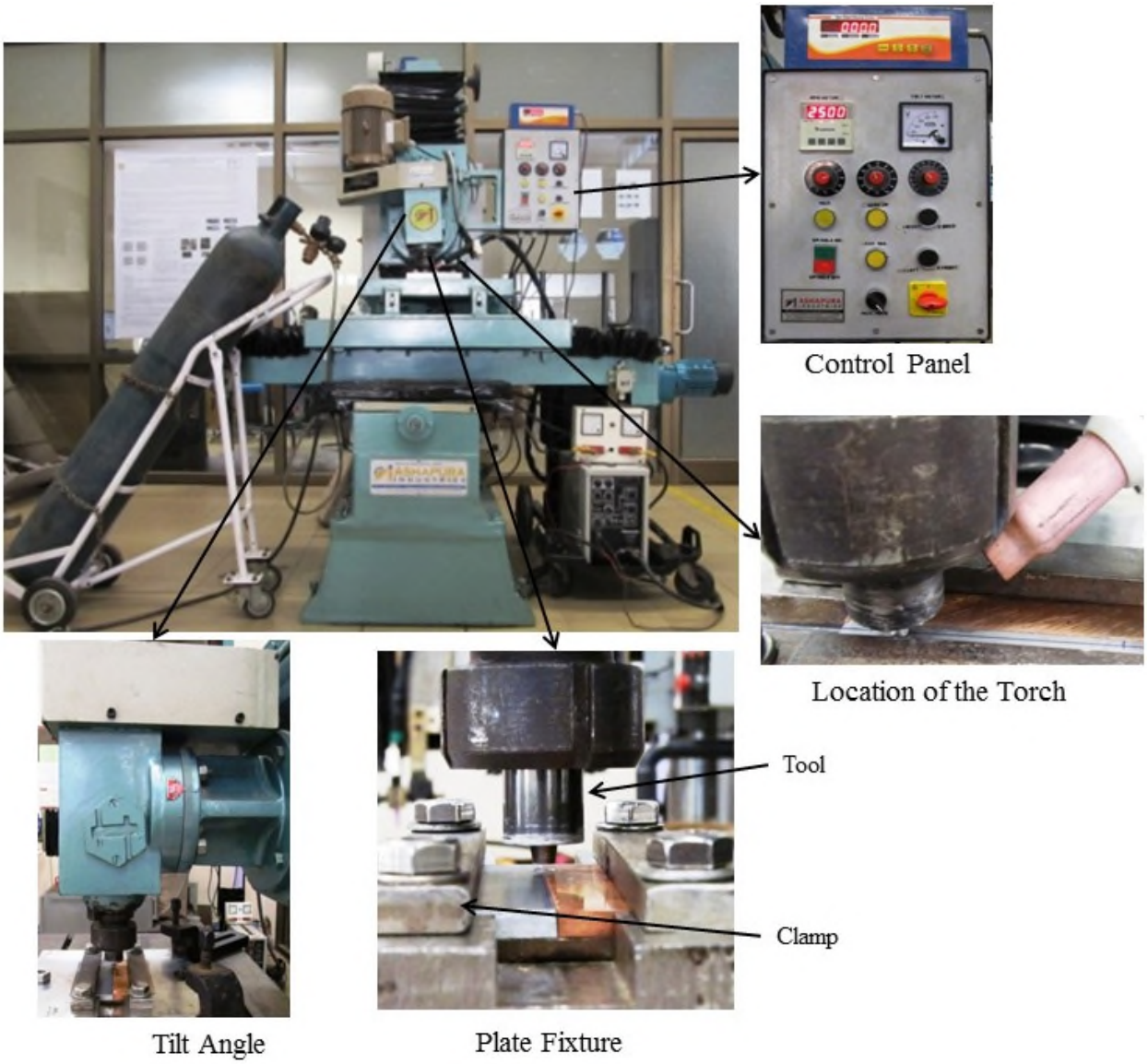

Figure 0.4. Overall experimental setup for friction stir welding.

1.14 Microstructural Evaluation

To perform the microstructural examination, the samples were cut from their respective plates. The cross-section of the samples was selected such that different zones formed during the welding process can be studied. Further, as a part of metallographic sample preparation, each sample was ground and polished to get a mirror-like surface finish. For primary grinding, 320, 500, 600, 800, 1200, 2000, and 4000 grade SiC emery papers were used. Later, the samples were polished using 3 μm MD Mol cloth with 3 μm MD Mol suspension and 1 μm MD Nap cloth with 1 μm MD Nap suspension. For the final step, the samples were kept in the VibroMet machine with colloidal silica suspension for 12-15 h. During the grinding and polishing steps, the orientation of samples was changed by 180° every time, and they were cleaned using a stream of cold water followed by alcohol and hairdryer to get rid of the impurities from the previous step.

1.14.1 Optical Microscopy

After using various etchants, it was observed that a solution consisting of 5 g NaOH, 2 g NaF, and 93 mL distilled water gave the best results. The optimum etching time was found out to be 1 minute. Etching for continuous one minute resulted in over-etching of the samples, so the polished surface of the samples was taken out of the etchant after 30 seconds and again dipped in the etchant after being thoroughly washed and cleaned. Various welding zones along with base metal were observed using a Nikon MA100 inverted microscope with Pax-it! Image analysis software. Images were taken at various magnifications from 50x to 1000x. Grain size calculations were performed using the in-built feature in PAX-it! which uses the intercept method. The optical microscopy setup is labeled in Figure 0.5.

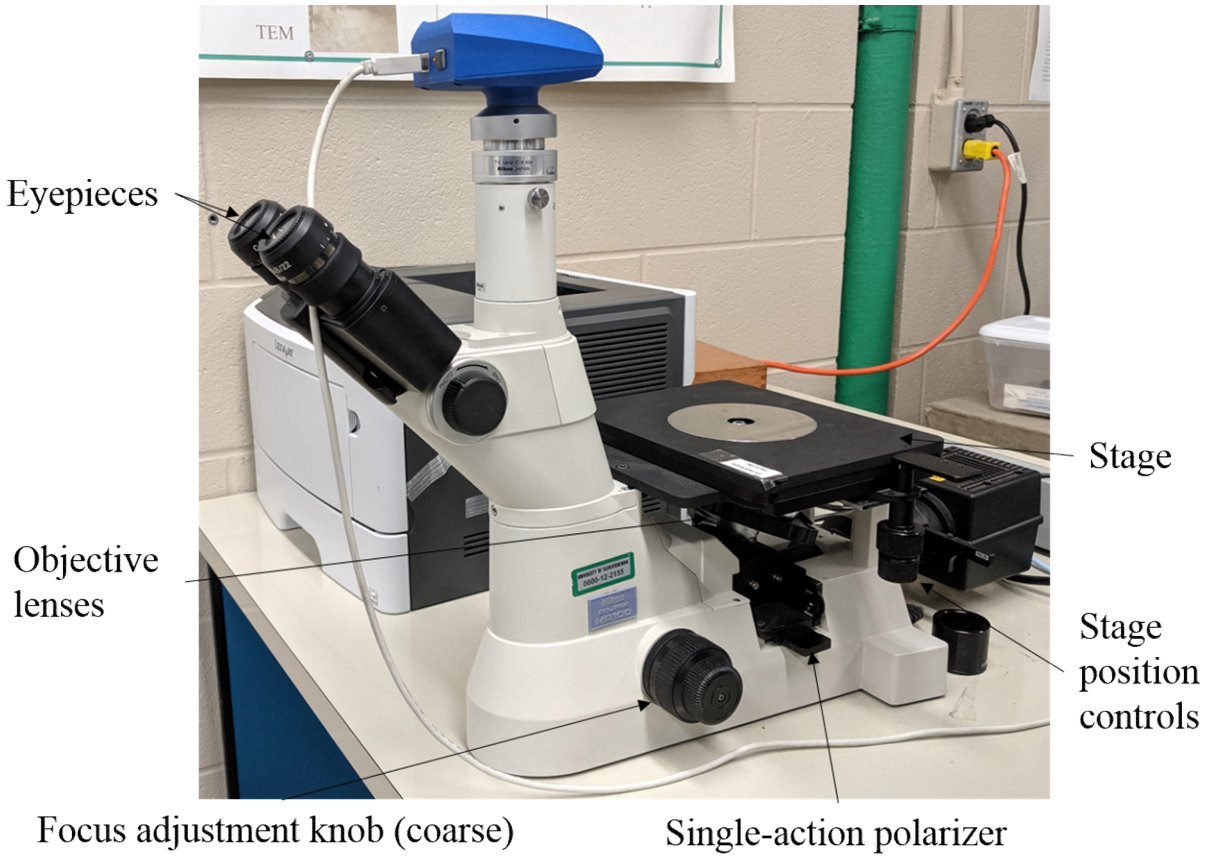

Figure 0.5. Nikon MA100 optical microscope.

1.14.2 Scanning Electron Microscopy (SEM) of Fractured Samples

Fractured samples after tensile test were observed under a SU 6600 Hitachi field emission scanning electron microscope to determine the mode of fracture/failure. The accelerating voltage used was 15 kV, and images at high resolution (2560×1920 pixels) were taken at different sites of interest at different magnifications (50x, 100x, 500x, and 1000x). Figure 0.6 shows the labeled picture of the equipment along with the EBSD detector attachment.

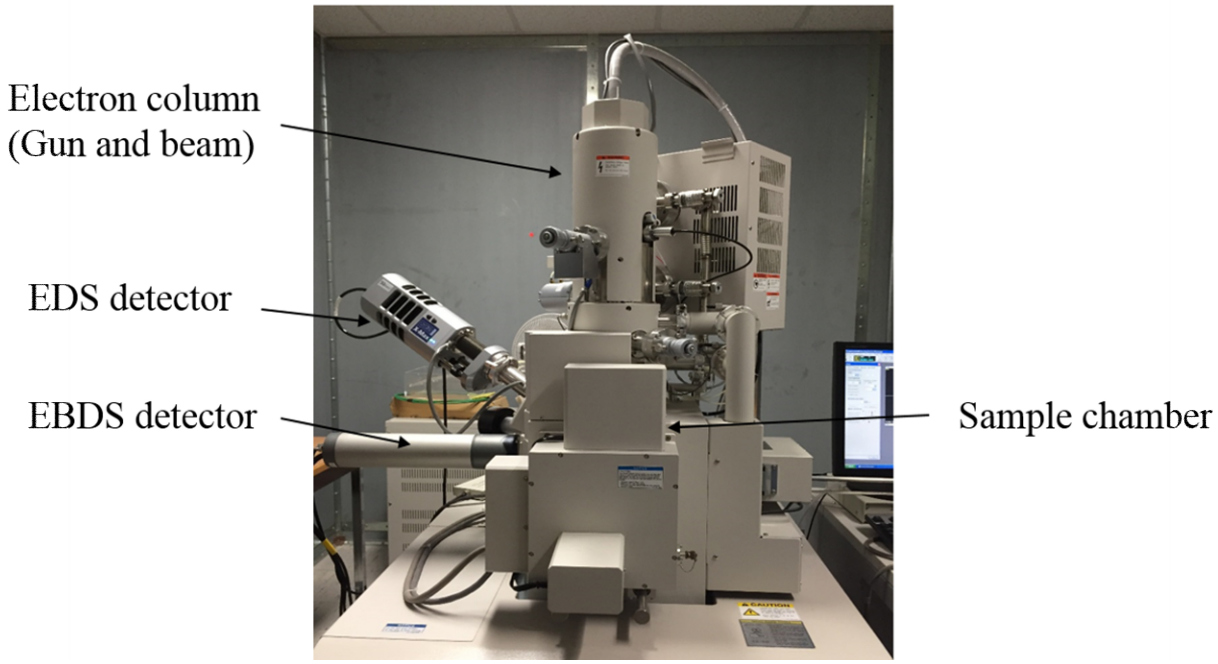

Figure 0.6. SEM and EBSD detector attachment.

1.14.3 Electron Back Scattered Diffraction Measurements

The highly polished samples were kept in a desiccator for 12 to 24 h before performing EBSD measurements to remove all the moisture or any kind of gas from the samples preventing the deflection of the electron beam from obtaining images without any noise. For optimal indexing, the samples were mounted on a stage using a carbon tape such that the samples formed 70° with the horizontal. EBSD was performed using a SU 6600 Hitachi field emission SEM equipped with an Oxford Instruments Nordlys EBSD detector. The data was acquired by AZTEC 2.0 data acquisition software in the form of backscattered electrons reflected on the phosphor screen detector. Scans at desired zones were performed at two magnifications: 100x and 400x. Frame average of 6 along with binning of 8x8 pixels was used to perform the scans at 30 keV energy. To obtain images with good resolution the step size were chosen to be 3 μm for 1.2 x 0.9 mm^2 area at 100x magnification and 0.31 μm for 0.3 x 0.2 mm^2 area at 400x magnification. The post-processing of the obtained scans was done using Channel 5 software by Oxford Instruments.

1.15 Hardness Measurement

The hardness profile of the welded samples was measured along the centerline of the weld cross-section using a Mitutoyo [MVK-H1] hardness testing machine, shown in Figure 0.7. The microhardness was measured by applying a load of 500 gf in the center of the weld for the dwell time of 10 seconds at an interval of 1mm along the transverse direction.

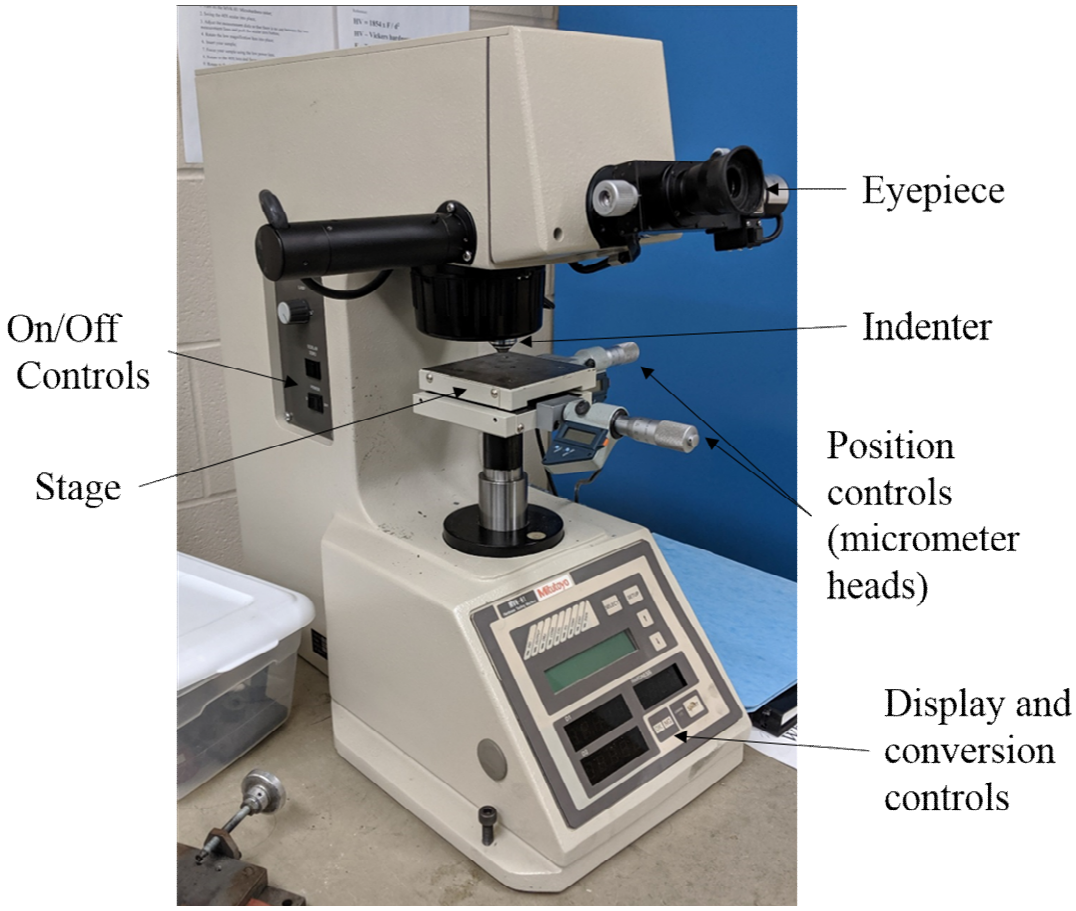

Figure 0.7. Mitutoyo MVK-H1 hardness testing machine.

RESULTS AND DISCUSSION

With the data obtained from microstructural observations and the mechanical tests, this chapter tries to explain the changes in microstructure and the resultant mechanical properties due to friction stir welding of the samples that were processed under different conditions. In the first section of this chapter, results obtained from optical microscopy are discussed. Data about grain boundaries, recrystallized fraction, and kernel misorientation, obtained from EBSD in various zones is presented and discussed in the second section of the chapter. The changes in hardness and tensile strength resulting from friction stir welding are discussed in the fifth and sixth sections. Results obtained from fractography are discussed in the fourth section of this chapter. In the last section, the effect of preheating or post-cooling on the overall microstructure and mechanical properties is discussed. Figure 0.1 shows the schematic of the weldment with different weld zones.

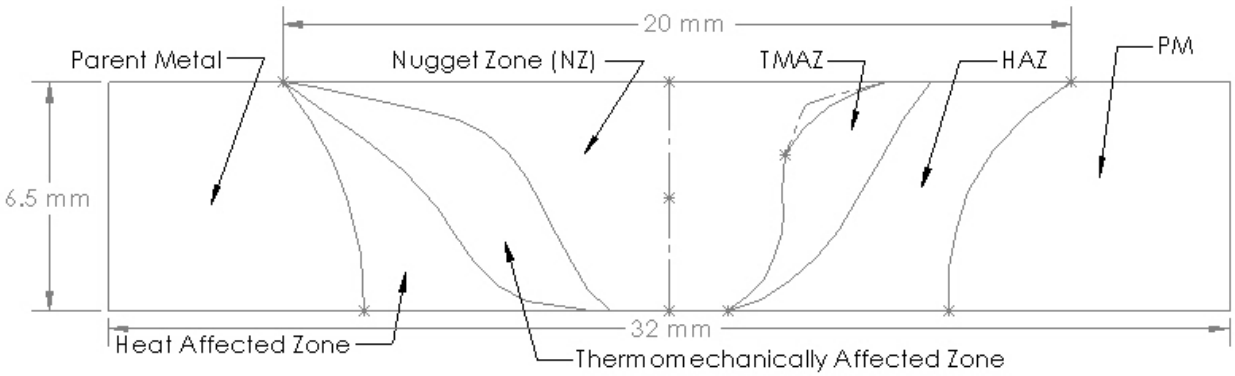

Figure 0.1. Different weld zones in friction stir welded sample (with approximate dimensions).

1.16 Effects of normal FSW

Optical Characterization:

Figure 0.2 shows an optical microscopy image of the parent metal region at 100X. It can be seen that the grains in this region are elongated along the horizontal direction (the direction in which the aluminum sheets were rolled). The grain size is around 100 μm.

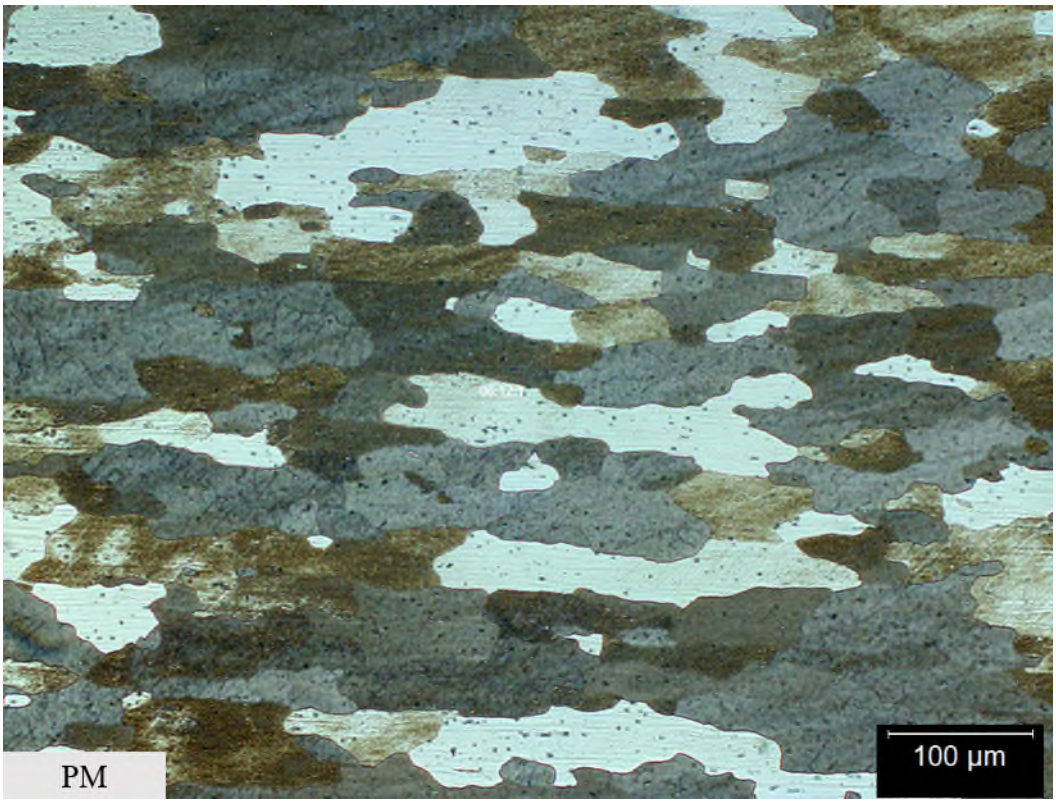

Figure 0.2. Parent metal region at 100X showing large elongated grains.

Looking at the lower magnification images (Figure 0.3) where the advancing and retreating sides are represented, it can be seen that the microstructure on both sides is asymmetrical. On the advancing side, the traveling and rotational force of the tool act in the same direction resulting in vortex-like features. On the other side, the direction of forces on the retreating side is opposite, resulting in lower forces compared to the advancing side [60].

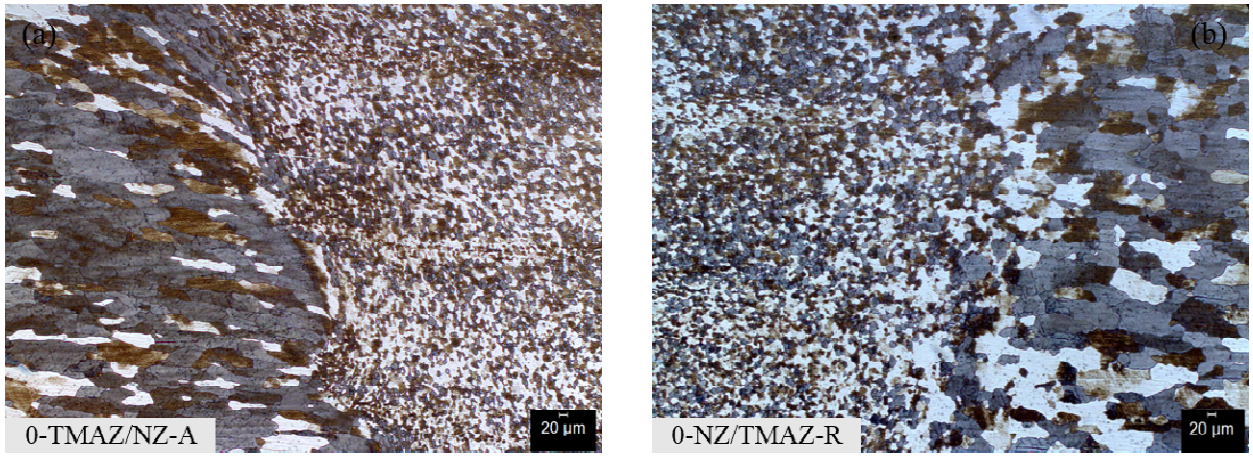

Figure 0.3. (a) Advancing side showing the transition from TMAZ to NZ, (b) Retreating side showing the transition from NZ to TMAZ, in FSW-0 sample at 50X.

In Figure 0.4 (a) and (b), it is seen that the grains in the top region are smaller in size compared to that in the center of NZ. Moreover, it should be noted that the grains near the top of the weld are more deformed and aligned in the direction parallel to the plate, whereas the grains near the root of the weld are equiaxed like in the center of the NZ. The top of the weld is in direct contact with the tool shoulder, and because of a lot of friction and pressure, the grains in this region are deformed differently. On the other hand, the root is in direct contact with the base plate, which helps to extract heat from the sample during and after the welding process, resulting in a higher fraction of recrystallized grains, which will be discussed later.

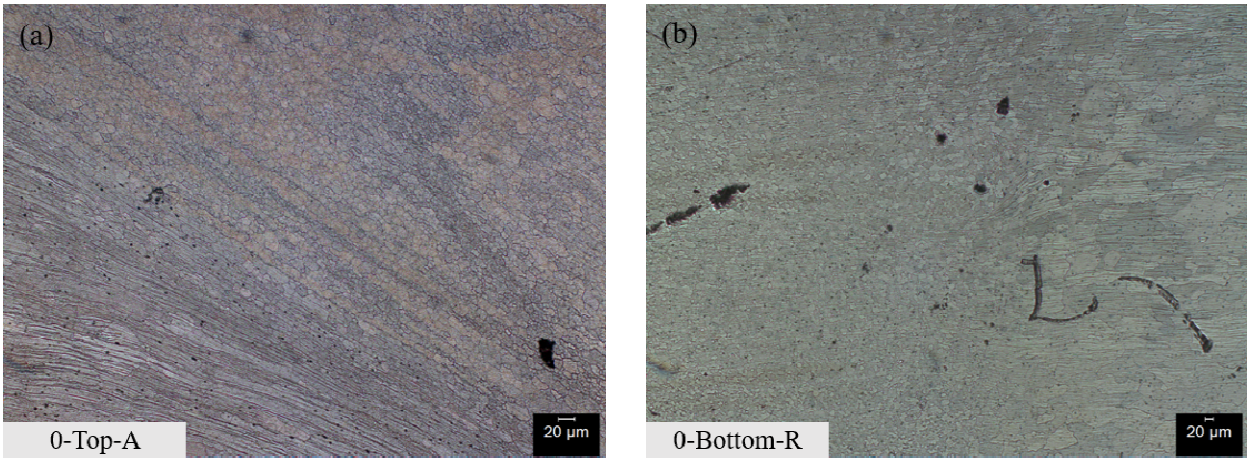

Figure 0.4. (a) Highly deformed region directly in contact with tool shoulder, (b) Equiaxed grains in the root region, in FSW-0 sample at 50X.

Grain boundaries:

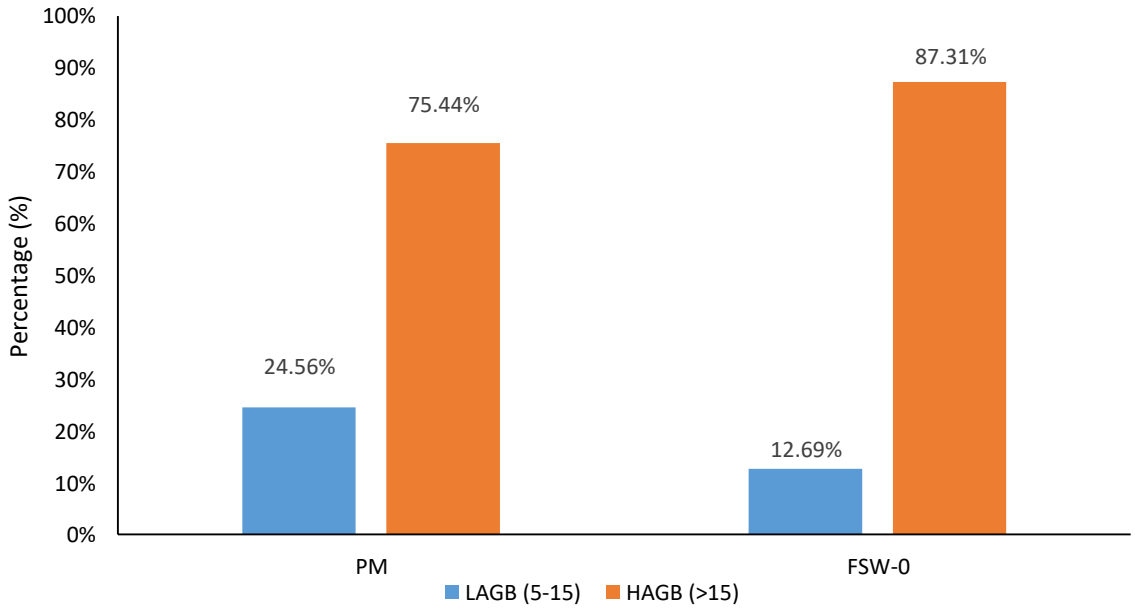

Figure 0.5. Percentage of LAGB and HAGB in the PM and the NZ of FSW-0 sample.

From Figure 4.5, it is seen that the fraction of LAGBs is higher in the parent metal compared to that in the weld center. Contrary to this, Figure 0.6 shows the opposite trend, which can be justified

by the fact that there is a significant difference in the grain size in the PM and the NZ. So, the relative frequency of the LAGBs in the PM is lower compared to that in NZ.

Comparing the grain boundary statistics of TMAZ AS & RS and HAZ, in Figure 0.7, it is seen that the fraction of low angle grain boundaries in TMAZ, especially on the RS, is much higher compared to that in the HAZ region. The percentage of grain boundaries with a misorientation angle of 8 in TMAZ AS and RS is 1.9 %, whereas in the HAZ is only 0.2 %. This means that the TMAZ region undergoes some plastic deformation along with exposure to the heat cycle during the welding process. In contrast, the HAZ region only undergoes a part of the heat cycle and shows similar grain boundary statistics to the PM.

Looking at the grain boundary statistics for a region near to the top of the cross-section in Figure 0.8, a similar trend is seen as in the TMAZ. This is the region where the shoulder of the tool is in direct contact with the sample, and so metal undergoes high plastic deformation resulting in a higher frequency of LAGBs. On the other hand, the root region of the weld center had fewer LAGBs as it is not in direct contact with the tool and hence does not undergo deformation as much as the top region. Also, most of the heat dissipation is through the root, which results in more recrystallized and equiaxed grains, contrary to more deformed grains observed in the top region of the weld center.

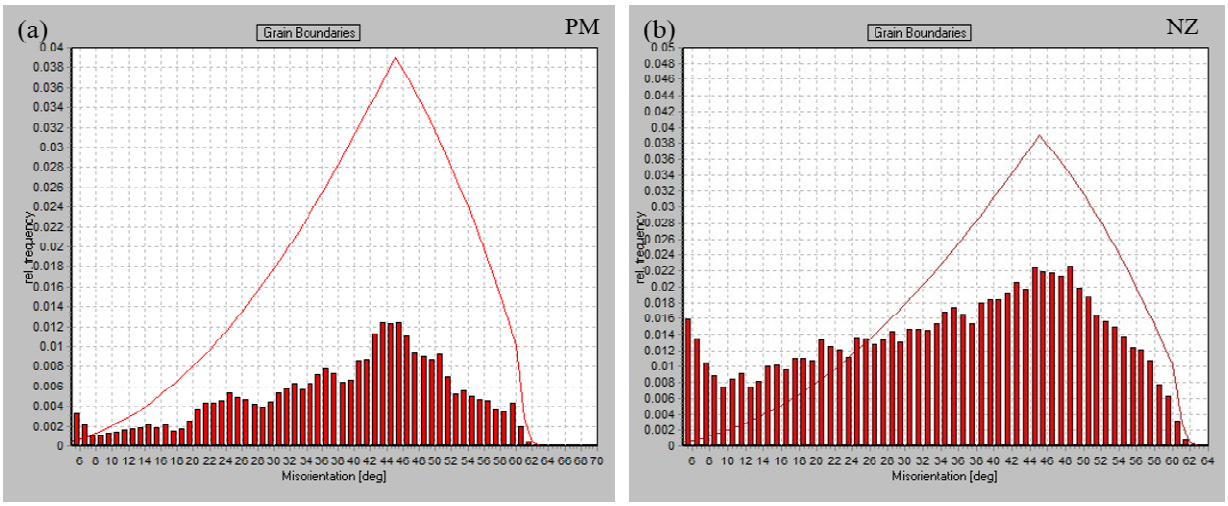

Figure 0.6. Grain boundary statistics in (a) PM and (b) the NZ of FSW-0 sample.

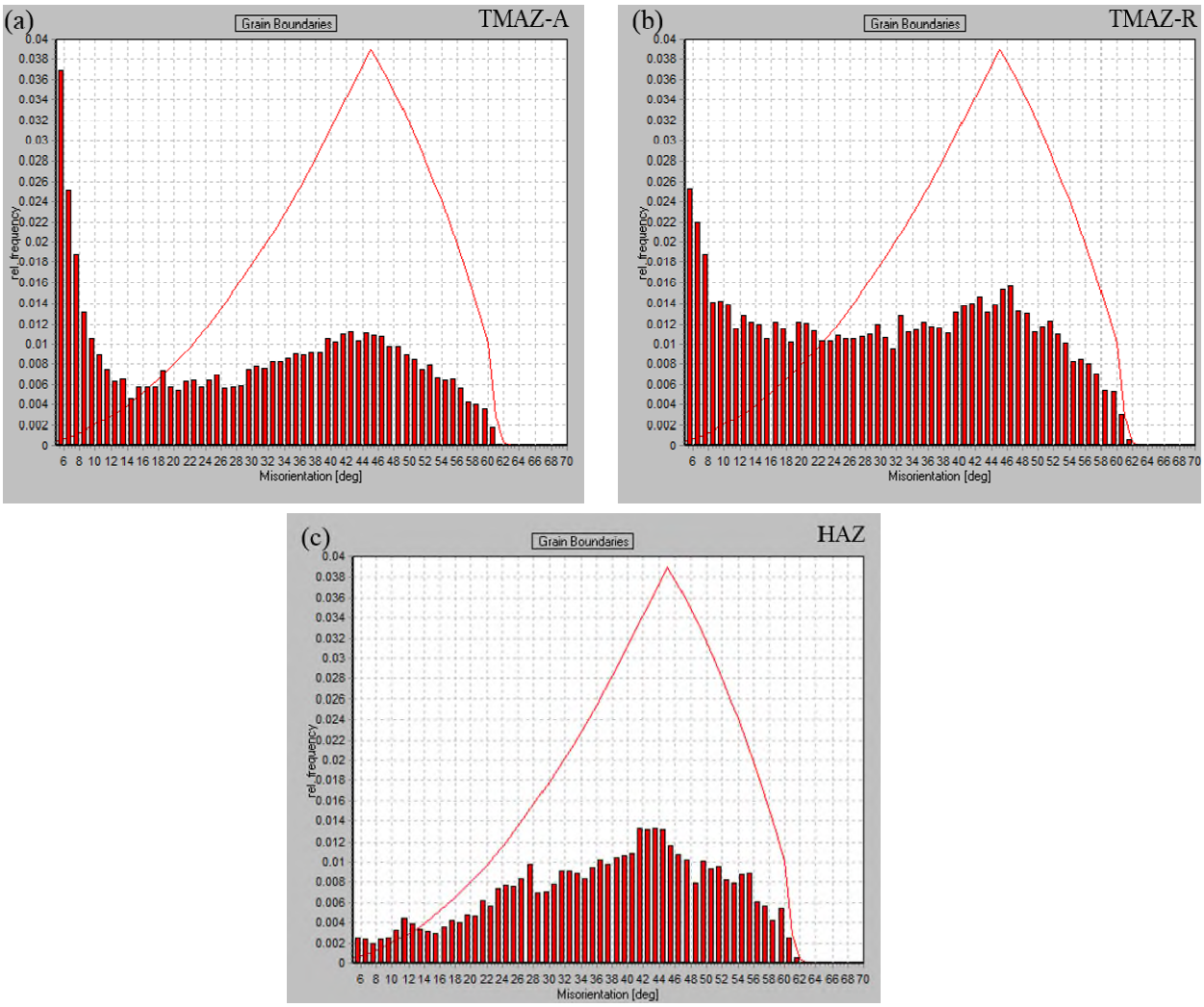

Figure 0.7. Grain boundary statistics for (a) TMAZ-A, (b) TMAZ-R and, (c) HAZ, for FSW-0 sample.

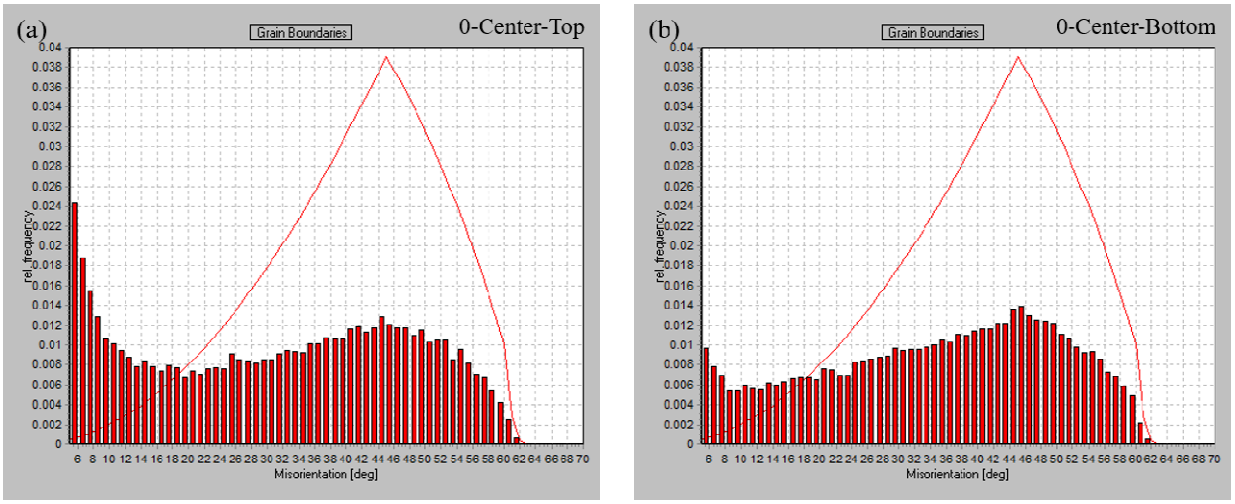

Figure 0.8. Grain boundary statistics for (a) Top, (b) Bottom of the NZ, of FSW-0 sample.

Kernel Misorientation

Kernel misorientation (KM) is used to represent small changes in orientation within the grains. A mean value is assigned to a pixel (highlighted in red in Figure 0.9 (a)) after the calculation of average misorientation between this pixel and its surrounding pixels (highlighted in yellow in Figure 0.9 (a)). Moreover, misorientations higher than 5º are neglected as they may represent the orientation in another grain. The process of calculating the misorientation is repeated for all the pixels on the map to create a KM map. Also, the intensity of local/kernel misorientation is illustrated by a rainbow color scheme, blue denoting negligible misorientation, whereas red displaying the highest misorientation (5º), as shown in Figure 0.9 (b). In Figure 0.10, it is seen that NZ has higher KM compared to that registered in the PM zone, and a similar trend has also been observed in Figure 0.5.

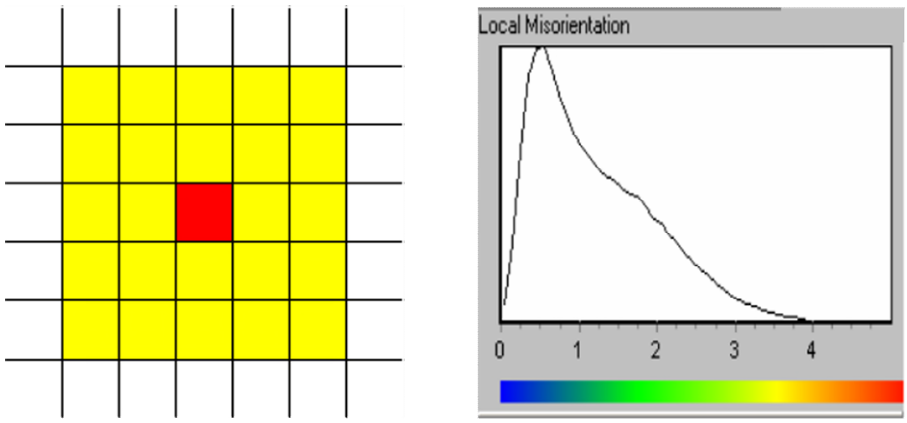

Figure 0.9. (a) Kernel misorientation concept, (b) Rainbow color scheme.

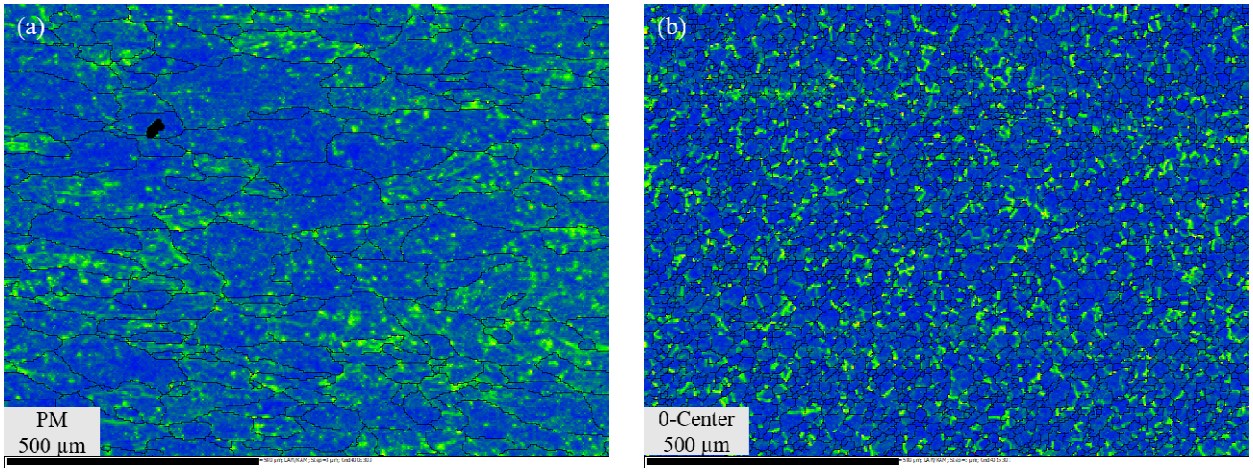

Figure 0.10. Kernel misorientation maps for (a) PM, (b) NZ having higher KM, of FSW-0 sample at 100x.

In Figure 0.11 (a) and (b), it can be seen that the top/crown region has higher KM, which is the result of severe plastic deformation resulting from the friction and pressure from the tool shoulder. In contrast, the root region has less KM as it is in direct contact with the base plate, and the grains undergo recrystallization.

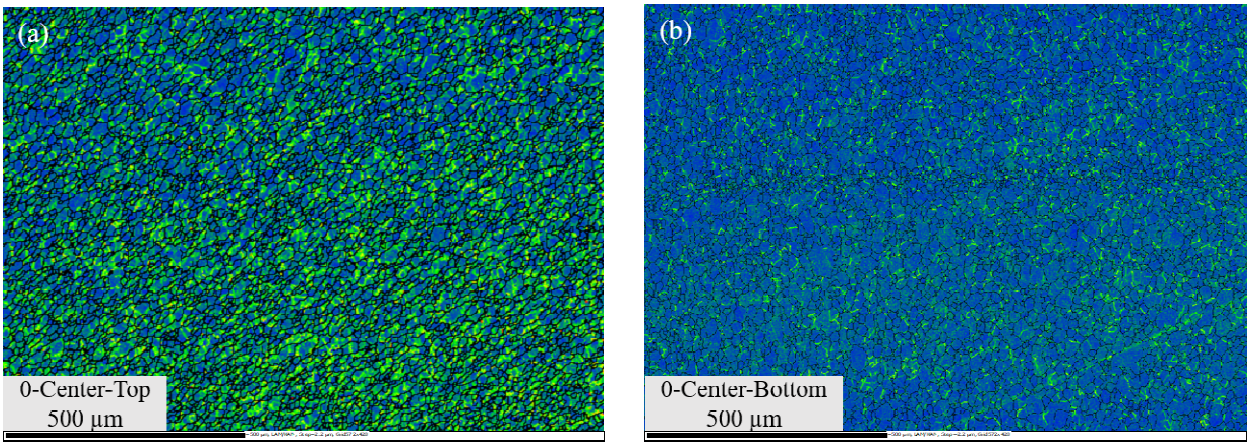

Figure 0.11. Kernel misorientation maps in the NZ (a) Top region with higher KM and (b) Bottom or root region with less KM, of FSW-0 sample at 100x.

Herrera [61] and Badji et al.[62] have concluded that the shift in peak from lower angle misorientation to higher angle misorientation is due to the increase in dislocation density. Figure 0.12 shows that the peak of the curve shifts by 1° in the PM towards higher Kernel because of the increase in dislocation density but is not so significant. The solution heat treatment and artificial ageing after the rolling maybe the reason for the insignificant increase in dislocation density.

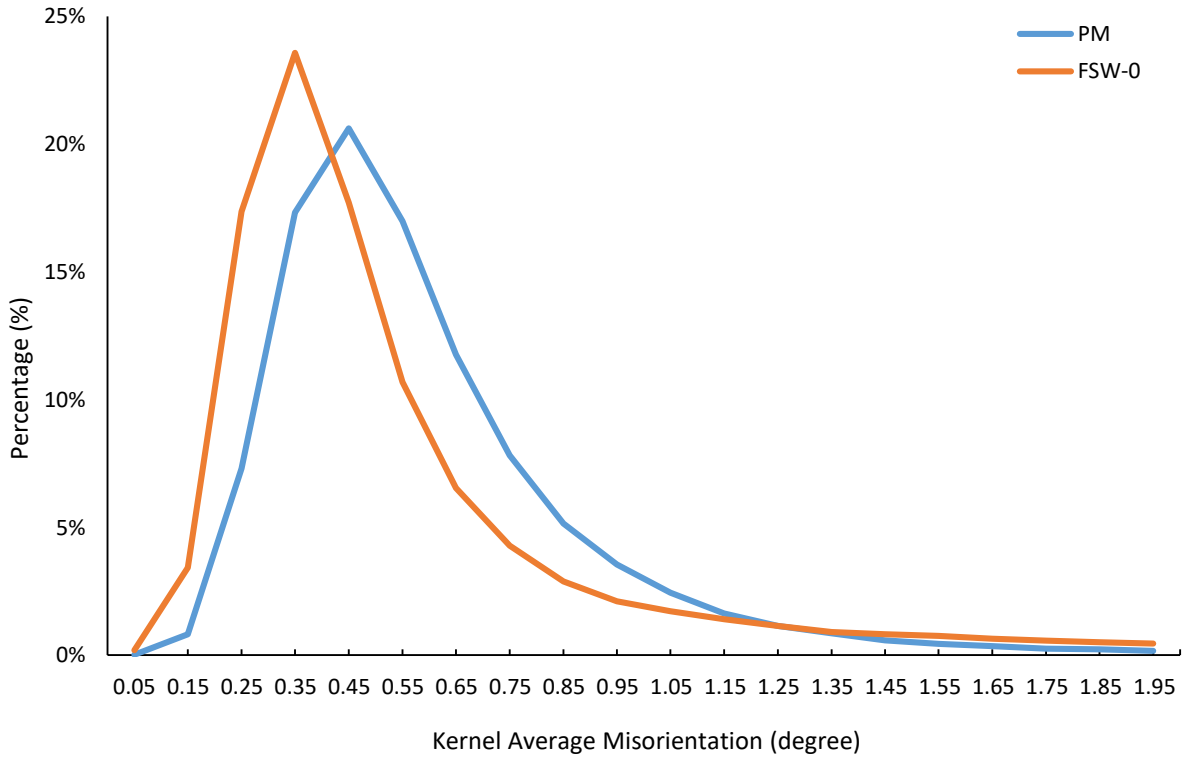

Figure 0.12. Kernel misorientation in the PM and the NZ of FSW-0 sample.

Recrystallized fraction

During the FWS process, the NZ, TMAZ, and some parts of HAZ undergo recrystallization due to high heat input and severe plastic deformation [37],[63]. Figures 0.13, 0.14, and 0.15 show the recrystallized fraction along with substructured and deformed fractions in various regions of the samples. The internal average misorientation (based on a specified misorientation angle of 5°) at each point in the grain is calculated after the reconstruction of grains takes place in the post-processing software. Now, if the average misorientation value of the point is less than that for subgrains (<0.5° here), the grain is defined as recrystallized. The grain is defined as substructured if the internal misorientation is <0.5° but the misorientation from subgrain to subgrain is >0.5°. All the grains where the average misorientation angle is >0.5° are termed as deformed grains. Moreover, the red, yellow and blue colors showing different recrystallized fractions also depict the amount of stored energy due to the dislocations, in a descending order of magnitude.

It is seen in Figure 0.13 (a) that the PM has a small fraction of deformed grains, which may due to the hot rolling process and solution heat treatment during the manufacturing of the aluminum plates [64]. The higher amount of substructured fraction in the PM can be the result of rapid recovery at high temperatures in aluminum, reducing the driving force for recrystallization [65]. The higher fraction of recrystallized and deformed grains in the NZ is the result of the heat cycle and plastic deformation occurring during the FSW process.

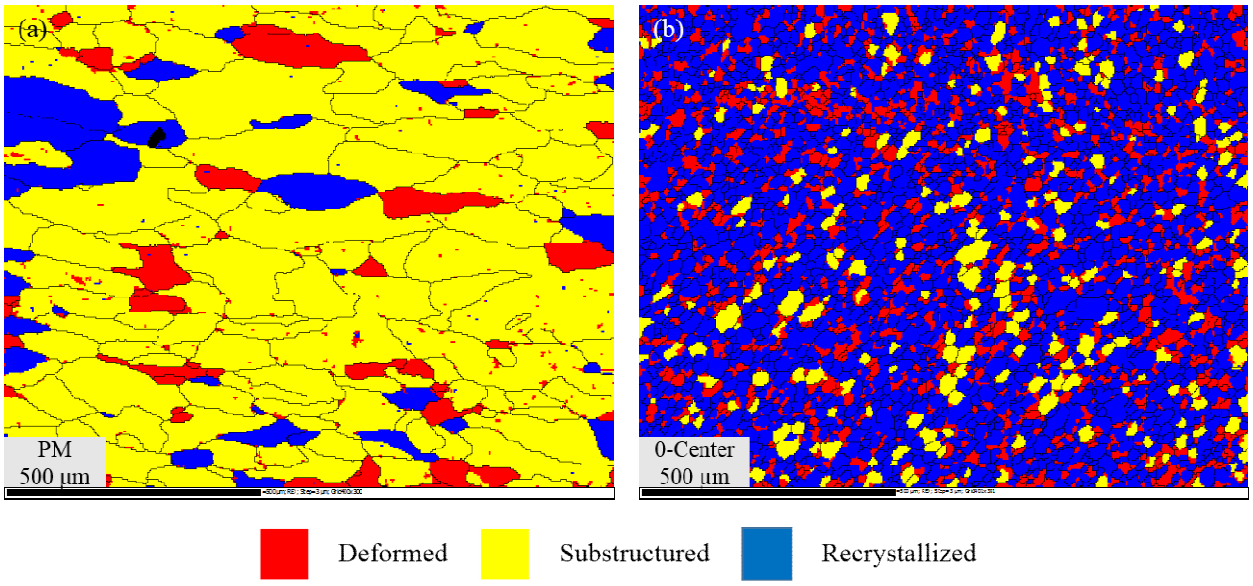

Figure 0.13. Recrystallized fraction maps for (a) PM with more substructured and deformed grains, (b) NZ with a higher number of recrystallized grains, of FSW-0 sample at 100x.

The amount of all the recrystallized fraction from NZ to TMAZ to HAZ can be seen in Figure 0.14. It is observed that the percentage of recrystallized grains is the highest in the NZ and the lowest in the HAZ. This indicates that the NZ grains undergo the highest amount of plastic deformation and the heat cycle. In the TMAZ region, the degree of recrystallization is less because of lower plastic deformation and lower temperature compared to that in NZ, as seen in Figure 0.14 (b). Comparing Figures 0.14 (c) and 0.13 (a), it can be said that HAZ and PM have a similar fraction of grains. HAZ has a bit more recrystallized grains because it is also exposed to a small part of the heat cycle during the FSW process.

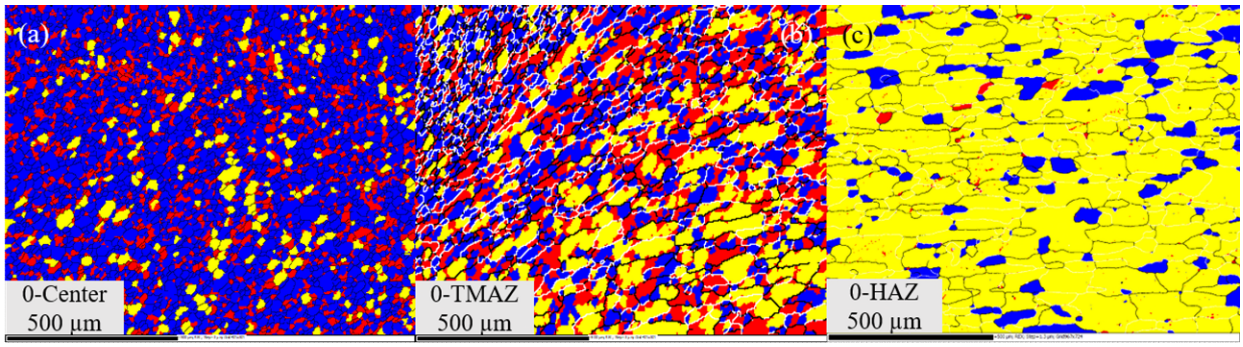

Figure 0.14. Transition of recrystallized fraction maps for (a) NZ, (b) TMAZ, and (c) HAZ, of FSW-0 sample at 100x.

Figure 0.15 shows the recrystallized fraction in the top and bottom regions of the NZ in the FSW-0 sample. It can be seen there that the amount of deformed grains is very high in the top region, whereas the amount of recrystallized grains is higher in the bottom region of NZ. A similar trend was observed in other samples as well. The higher fraction of deformed grains at the top is because the top part of the sample is always in direct contact with the tool. Hence, it undergoes severe plastic deformation, and cooling is accelerated. The bottom part of the weld undergoes recrystallization because of the temperature gradient between the top and bottom.

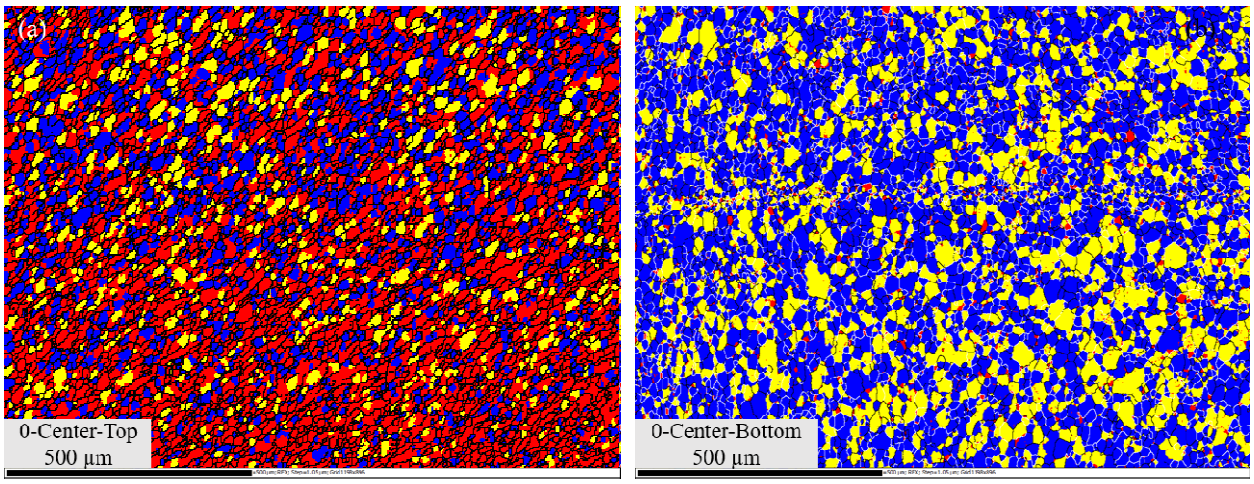

Figure 0.15. Recrystallized fraction maps in the NZ (a) Top and (b) Bottom of FSW-0 sample, at 100x.

Gurao et al. [66] used kernel misorientation to correlate misorientation within the microstructure to the degree of plastic deformation and concluded that dislocations accumulate in sub-grain boundaries, which eventually coalesce to form nuclei of new grains. Figure 0.16 shows the recrystallized fraction and kernel misorientation maps of the NZ/TMAZ. It can be seen that the regions with higher kernel misorientation in Figure 0.16 (b) are labeled deformed in Figure 0.16 (a), the ones with the least kernel misorientation are labeled as recrystallized and the regions with moderate kernel misorientation are substructured or recovered.

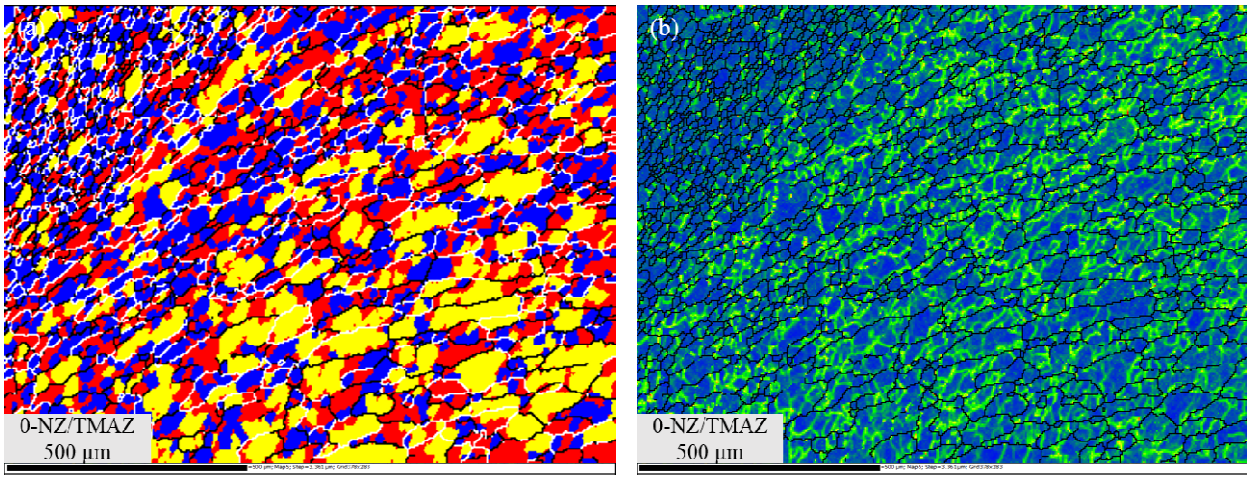

Figure 0.16. (a) Recrystallized fraction map for NZ/TMAZ and (b) Kernel misorientation map for NZ/TMAZ of FSW-0 sample, at 100x.

1.17 Effects of preheating

Optical Characterization

In the preheated samples, the grains from TMAZ transit into NZ where they are slightly elongated parallel to the surface of the sheet, compared to the samples prepared under other conditions as shown in Figure 0.17, this may be due to slightly higher heat input compared to the as-welded samples because of the preheating applied before the welding.

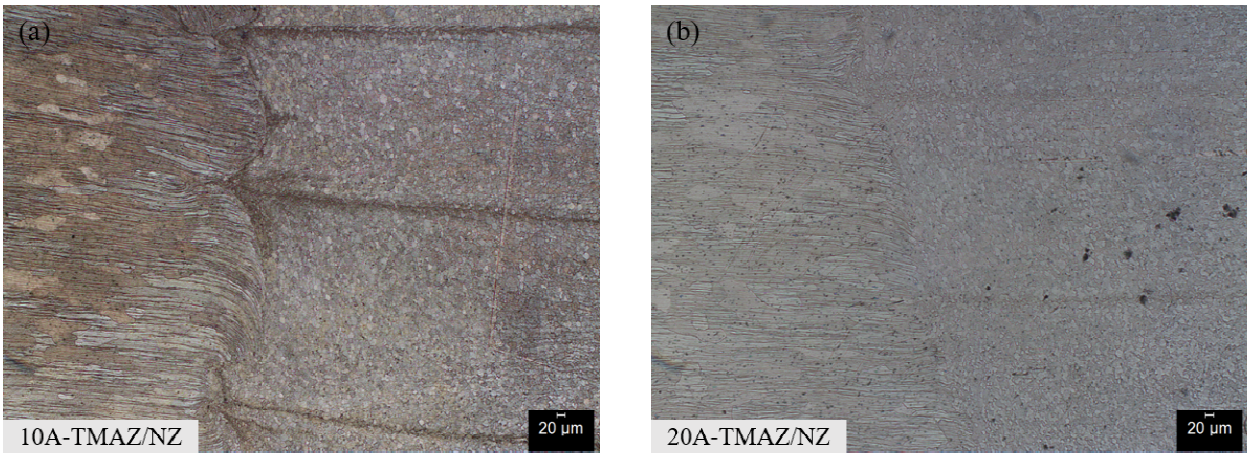

Figure 0.17. Advancing side, (a) TMAZ/NZ region in FSW-10A sample, (b) TMAZ/NZ region in FSW-20A sample, at 50x.

In Figure 0.18, it is seen that the interface of NZ and TMAZ on the retreating side is not as well defined compared to the as-welded and post cooled samples.

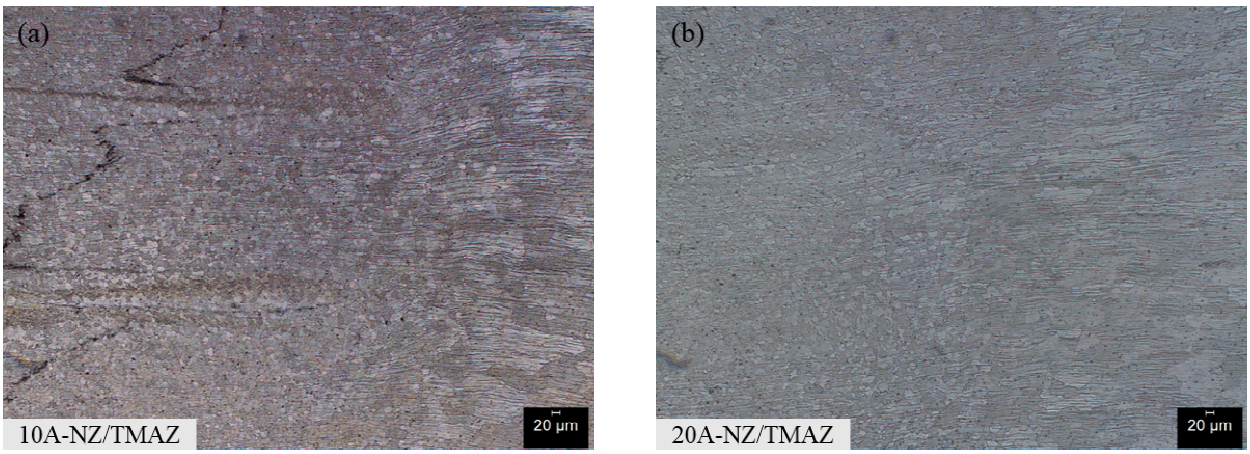

Figure 0.18. Retreating side, (a) NZ/TMAZ region in FSW-10A sample, (b) NZ/TMAZ region in FSW-20A sample, at 50x.

An array of zig-zag lines is observed in Figure 0.18 (a). According to Sato et al. [67] and Okamura et al. [68], these are oxides mainly Al_2O_3, which are present on the surface of aluminum alloys and have not been destroyed during the welding process. Usually, these oxides do not affect the mechanical properties. On the contrary, Zhou et al. [69] have reported that when the depth of

penetration is less and such oxides are formed from the root, it results in a root flaw, also known as “kissing bond” which reduces the fatigue life of welds by 20-30 times. Evidence of fracture due to the oxide particles is seen in Figure 0.19. It shows that the fracture took place in NZ with the features resulting from the oxide lines. A similar fracture occurred in some of the FSW-0, and both post cooled samples.

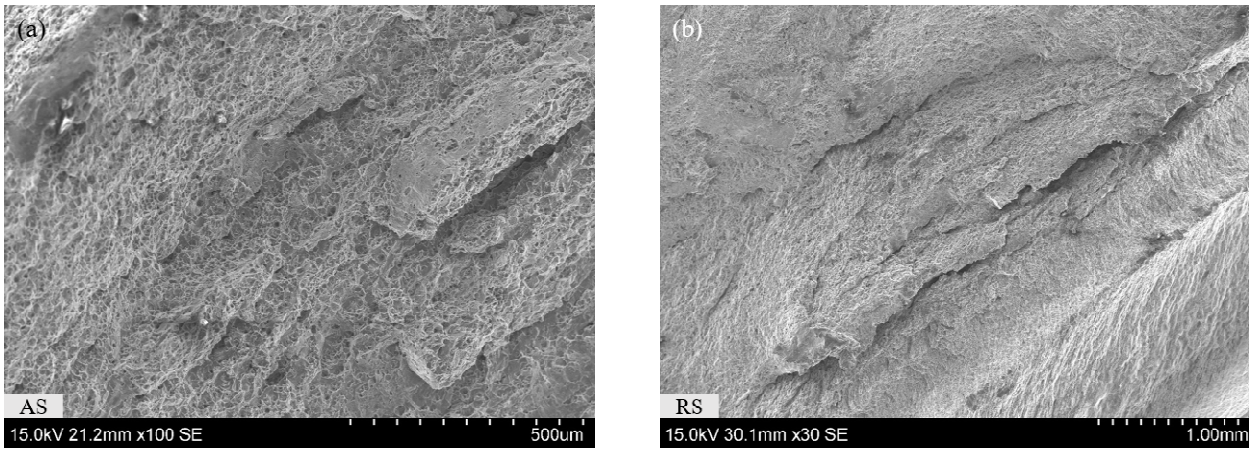

Figure 0.19. Fracture surfaces of FSW-10A showing brittle failure from the NZ.

Grain boundaries

When comparing the statistics of grain boundaries in the as-welded sample and preheated samples in Figure 0.20, it can be seen that there was no significant change in the percentage of grain boundaries with increasing the preheating temperature.

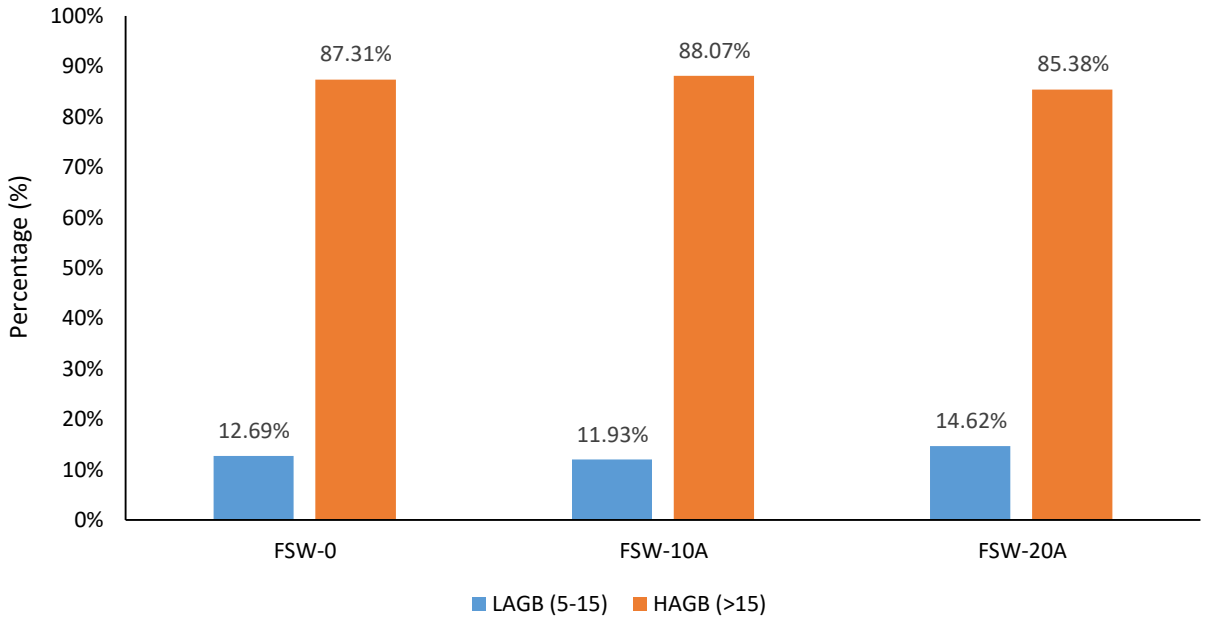

Figure 0.20. Percentage of LAGB and HAGB in the NZs of FWS-0 sample and the preheated samples.

Kernel Misorientation

Figure 0.21 shows the kernel misorientation maps of preheated samples. It is seen that the areas near the flow lines have lower misorientation, and grains are more often recrystallized. This is because they underwent higher plastic deformation, and there was higher heat input resulting in a higher fraction of recrystallized grains.

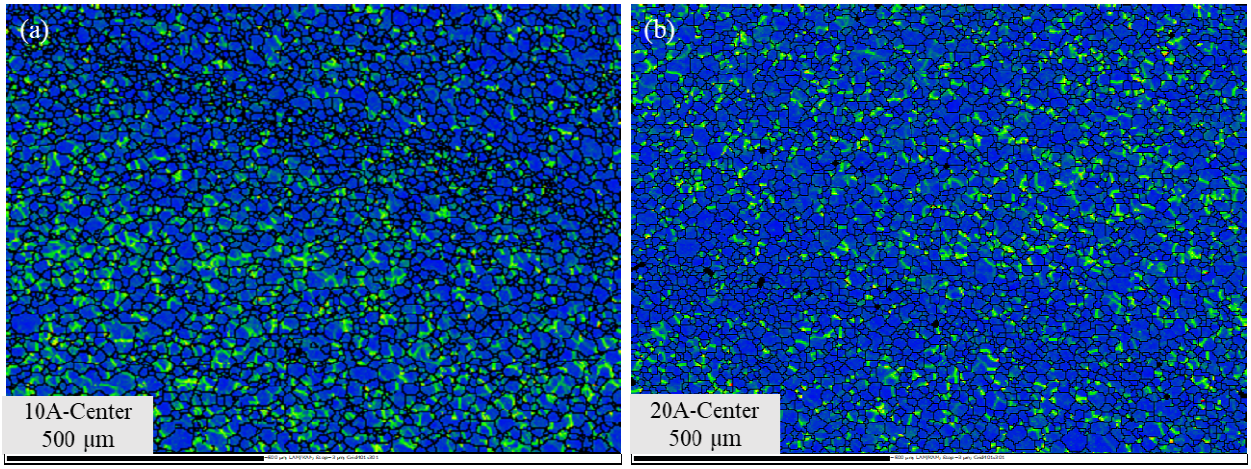

Figure 0.21. Kernel misorientation maps for the NZs of (a) FSW-10A, and (b) FSW-20A samples; at 100x.

Similar to Figure 0.10, there is no significant change in kernel misorientation in preheated samples compared to the FSW-0 sample, as seen in Figure 0.22. However, it should be noted that the dislocation density decreased with the preheating, and the difference in heat input between FSW-10A and FSW-20A samples is not enough to affect the dislocation density and Kernel misorientation in the NZ.

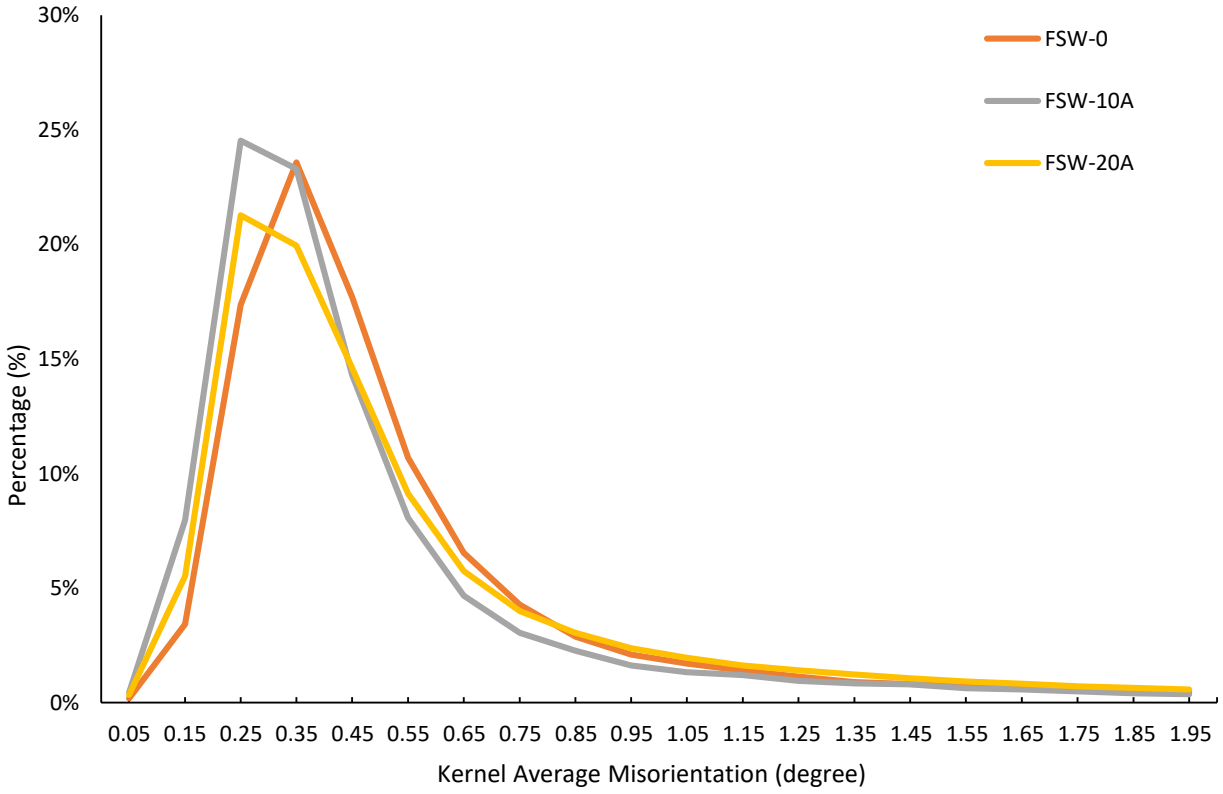

Figure 0.22. Kernel Misorientation in the NZs of preheated samples.

Recrystallized fraction

As shown in Figure 0.23, most of the grains in both samples are recrystallized. Preheated samples have a higher fraction of recrystallized grains because they are exposed to comparatively higher temperatures than post cooled and FSW-0 samples.

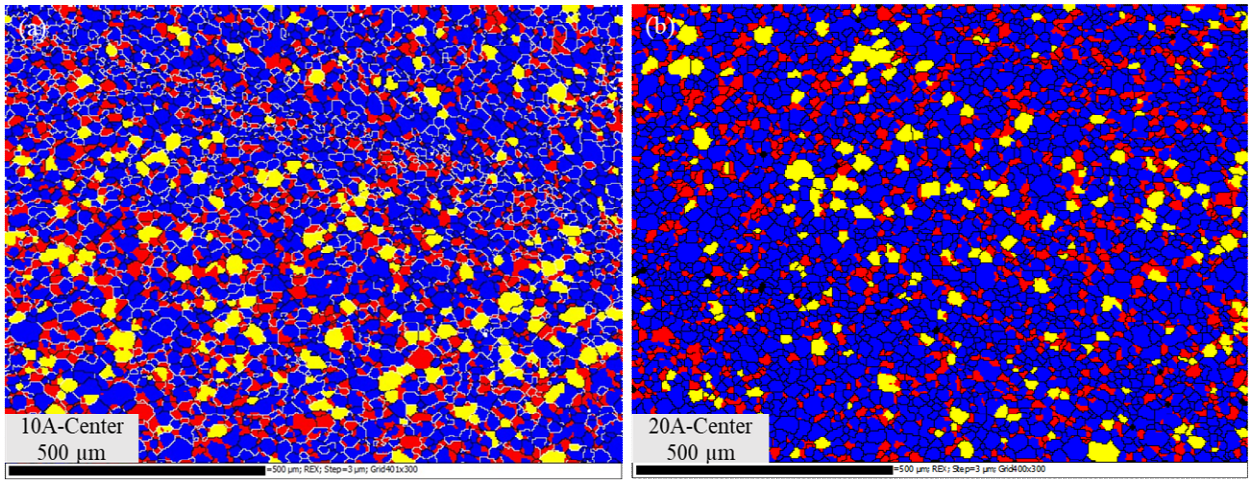

Figure 0.23. Recrystallized fraction maps for the NZs of (a) FSW-10A, and (b) FSW-20A samples, at 100x.

1.18 Effects of post-cooling

Optical Characterization

Figures 0.24 and 0.25 show the optical micrographs of the advancing and retreating side of the post cooled samples. On the advancing side, the grains at the interface are also elongated but are comparatively shorter than those found in the preheated samples. Moreover, the transition from NZ to TMAZ is well defined in these samples, which is not the case at the interface of the NZ and the TMAZ on the retreating side.

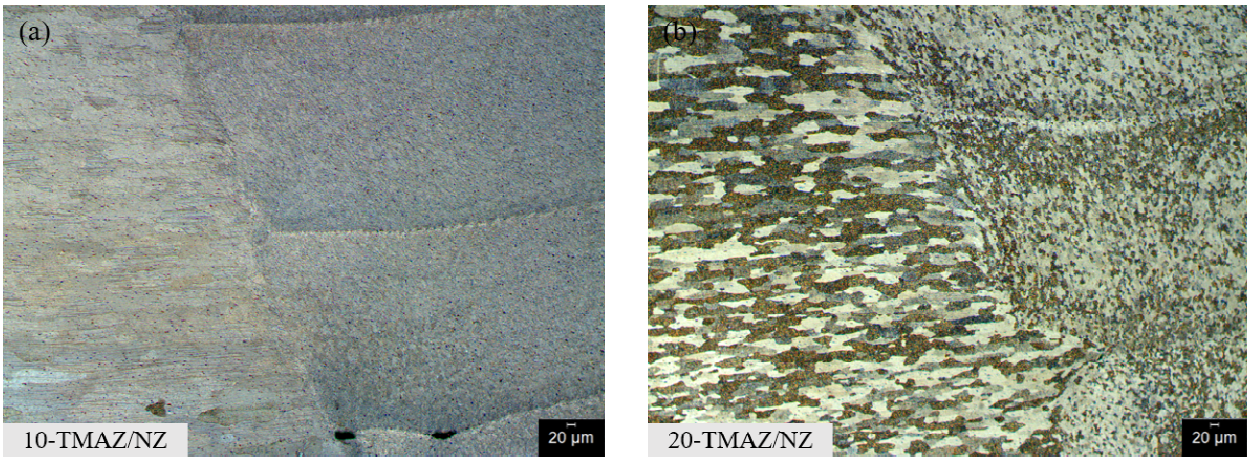

Figure 0.24. Advancing side, (a) TMAZ/NZ region in FSW-10 sample, (b) TMAZ/NZ region in FSW-20 sample, at 50x.

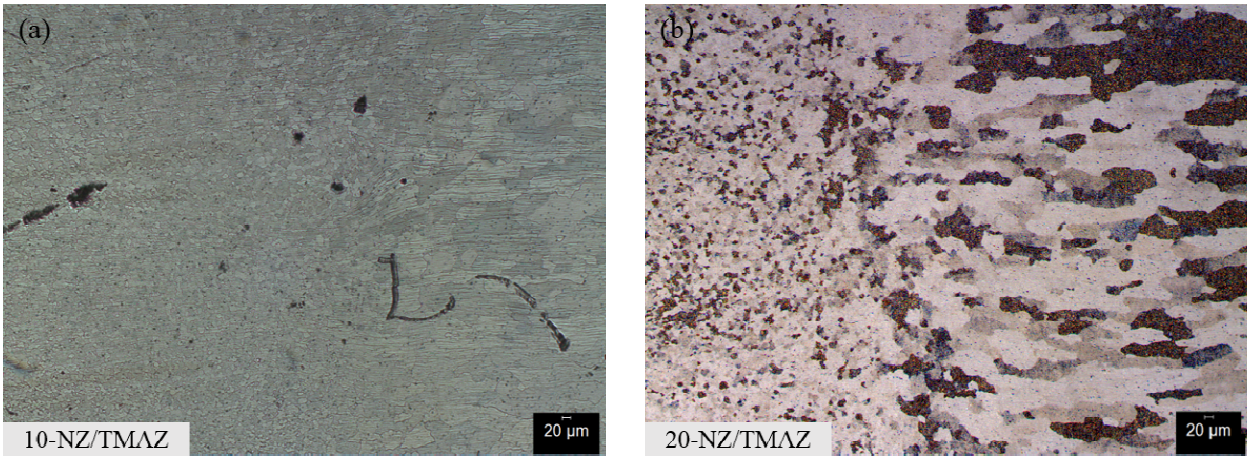

Figure 0.25. Retreating side, (a) NZ/TMAZ region in FSW-10 sample, (b) NZ/TMAZ region in FSW-20 sample, at 50x.

In Figures 0.17 and 0.24, one can see flow lines that are dependent on the tool design, dimensions, and welding parameters [70]. It should be noted that the flow lines which are very clear in the advancing side are hardly visible in the retreating sides of the same samples, Figures 0.18 and 0.25. It is seen that these flow lines are related to two different material flow currents proven by a simulation study, one of which is responsible for depositing the material directly behind the tool after picking it up from the front in the retreating side. In contrast, the other current is responsible for the downward or upward flow of the material, depending on the direction of the threads [71].

Similar to Figure 0.19, Figure 0.26 shows the fracture in the NZ of the FSW-10 and FSW-20 samples, probably because of the oxide formation in NZ.

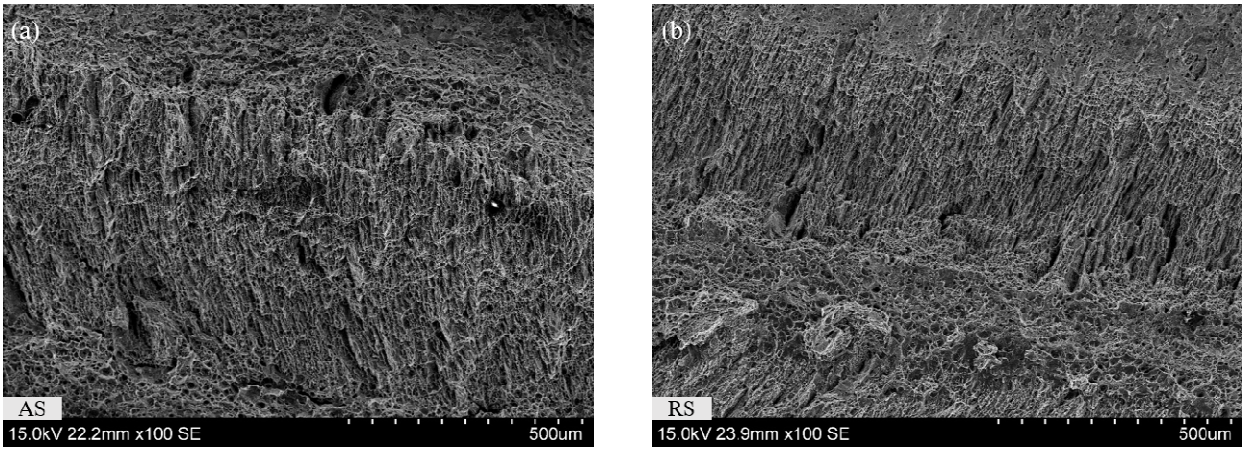

Figure 0.26. Fracture surfaces of FSW-10 sample showing brittle failure from the NZ.

Grain Boundaries

No significant difference in the grain boundary percentage was observed between the FSW-0 samples and the post cooled samples as shown in Figure 0.27.

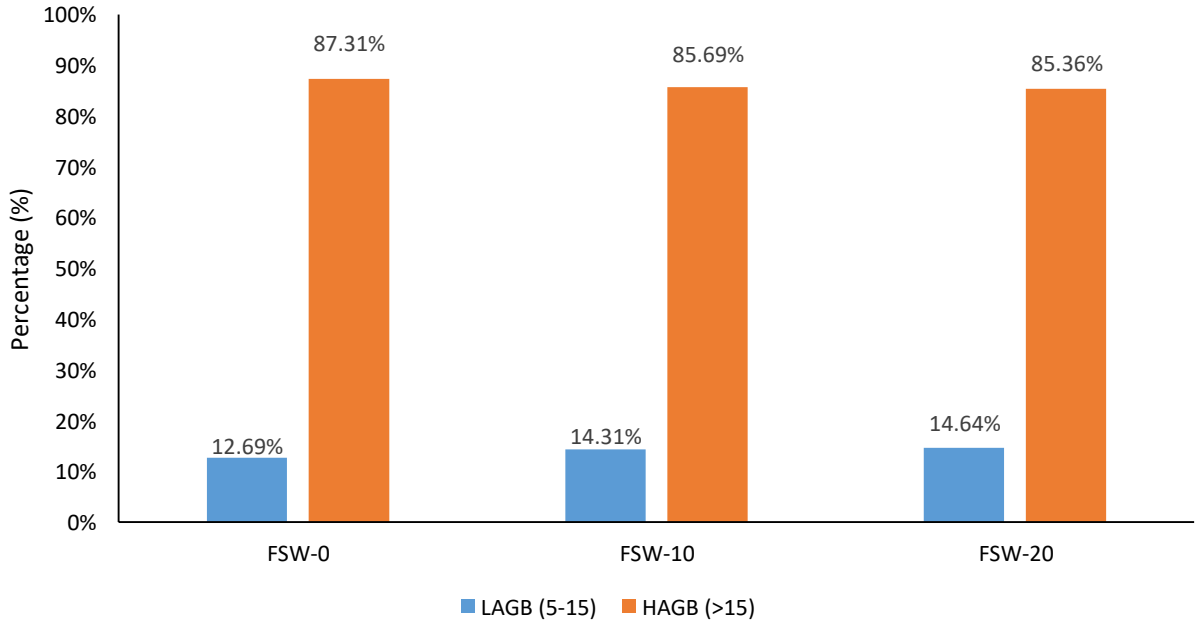

Figure 0.27. Percentage of LAGB and HAGB in the NZ of FSW-0 and the post cooled samples.

Kernel Misorientation

Figure 0.28 shows that the NZ of FSW-20 sample has slightly higher Kernel misorientation compared to that of the FSW-10 sample.

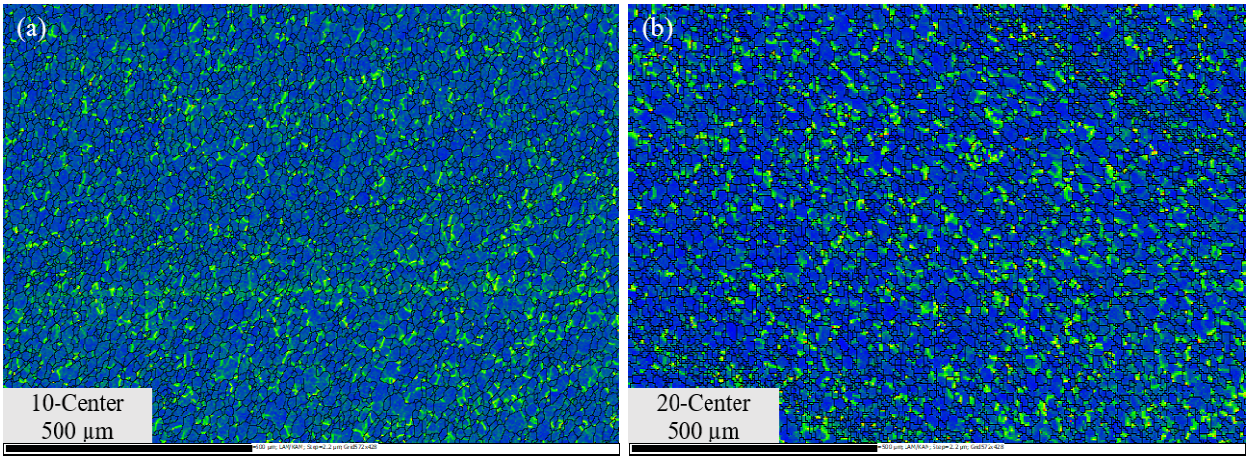

Figure 0.28. Kernel misorientation maps for the NZs of (a) FSW-10, and (b) FSW-20 samples; at 100x.

Overall cooling effect results in an increase of dislocation density in the NZ, as shown in Figure 0.29. However, the difference in dislocation density between the post cooled samples is negligible. When comparing Figures 0.22 and 0.29, measurable differences in the dislocation density can be seen, and this can explain the difference in the percentage of deformed grains in the respective samples.

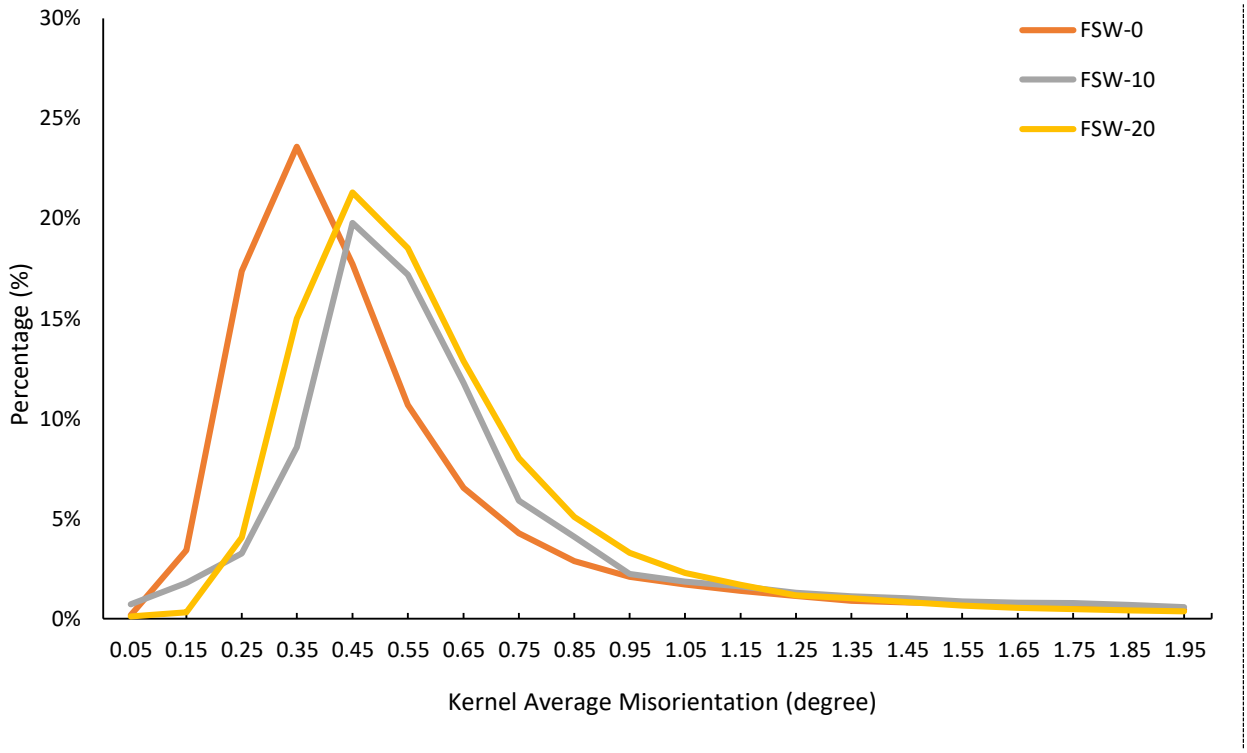

Figure 0.29. Kernel misorientation in the NZs of post cooled samples.

Recrystallized fraction

Figure 0.30 shows that there is a slightly higher number of substructured and recrystallized grains in the FSW-10 sample. A higher cooling rate in the FSW-20 sample reduces the fraction of recrystallization and recovered grains, resulting in a higher number of deformed grains. Higher Kernel misorientation in the NZ of FSW-20 (as seen in Figure 0.28) can be justified by the increase in cooling effect resulting in a higher percentage of deformed grains in Figure 0.30.

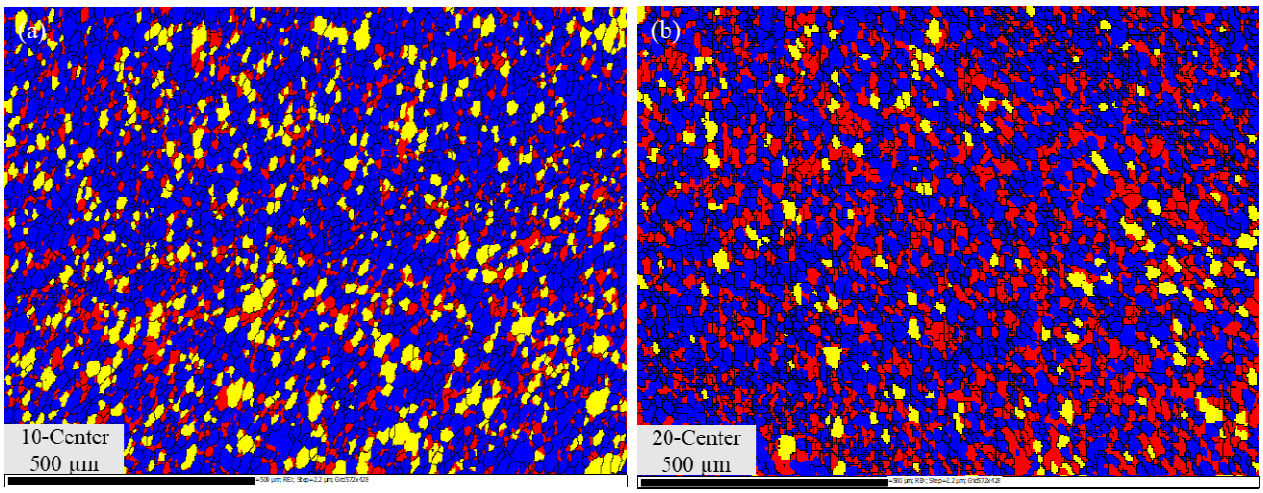

Figure 0.30. Recrystallized fraction maps for the NZs of (a) FSW-10, and (b) FSW-20 samples; at 100x.

1.19 Effect on Grain Size

During the FSW process, the samples undergo heat cycles along with plastic deformation, resulting in significant changes in the grain size in the respective weld zones depending on the exposure to heat and deformation. The average grain size in PM was found out to be around 98 µm. In the NZ, the average grain size of FSW-0 samples was 12 µm, the least being 8 µm in FSW-20 and highest being 14 µm in FSW-20A samples. The average grain size in HAZ of post cooled samples were 69 µm, whereas in that of the HAZ of preheated samples was 77 µm. The highest average grain size (117 µm) was observed in the HAZ of the FSW-20A sample. The larger grain size in preheated samples is due to the slower cooling rate compared to those in FSW-0 and post cooled samples. So, the grains in HAZ undergo grain growth over a more extended period and coarsen because of higher temperatures resulting in larger grains.

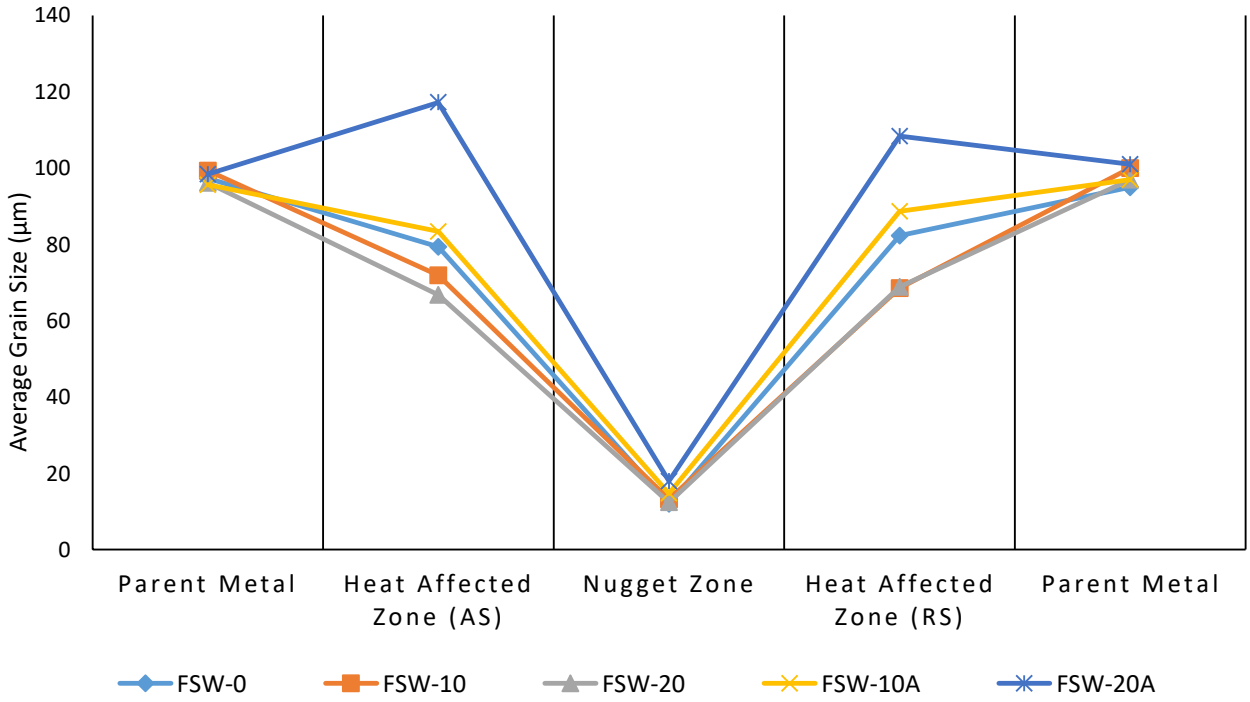

Figure 0.31. Average grain size in various weld zones.

Overall, it is seen that the PM has the largest grains, and NZ has the smallest grains. The grain size trend is PM>HAZ>TMAZ>NZ. This trend is because of the temperature gradient and the extent of deformation in various zones. The parent metal does not undergo any deformation or heat cycle, whereas the NZ undergoes severe plastic deformation resulting is small grains and the highest temperature producing equiaxed and recrystallized grains.

1.20 Hardness

Hardness in precipitation hardening alloys depends mainly on grain size, dislocation density, precipitate distribution, and accumulated residual stresses. These factors get changed based on the peak temperature, the duration of the heat cycle, and the plastic deformation experienced by various weld zones. Figure 0.32 shows the hardness profile across the FSW-0 samples with the hardness of parent metal as a reference. The highest hardness value of 107 VHN is seen in the PM, whereas the HAZ has the lowest hardness value of 53.5 VHN. In NZ, the highest hardness value reaches 83.5 VHN.

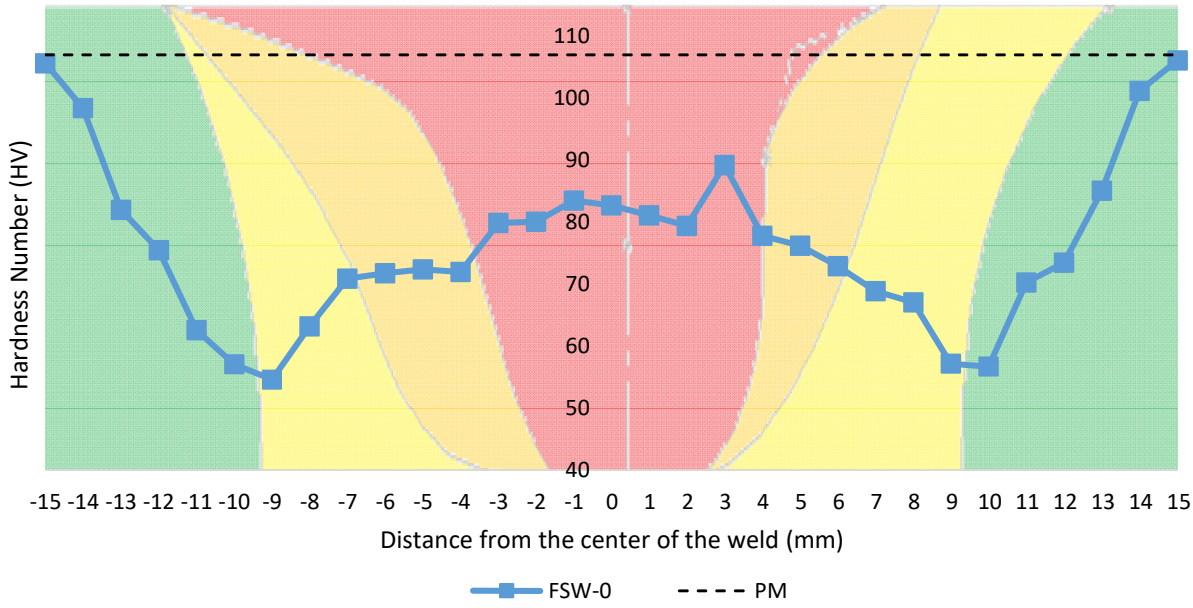

Figure 0.32. Hardness in parent metal vs FSW-0 (Red- NZ, orange- TMAZ, yellow- HAZ and green- PM).

The HAZ has the lowest hardness values, even if the average grain size is between 60-100 µm. Heinz [72] and Fonda et al. [73] observed that coarsening of precipitates takes place in HAZ, which results in the weaker region.

It is seen that the NZ has lower hardness compared to the PM, even if the grain size is the smallest. This maybe because of the thermal history of Al 6061 which creates a softened region around the weld center [72]. Sato et al. showed that various weld zones undergo different heat cycles based on varying peak temperatures. It was observed that the temperature of around 400 °C was responsible for the dissolution of precipitates in NZ, which then reprecipitate during the cooling period. The TMAZ and HAZ undergo similar heat cycles but with lower peak temperatures resulting in the dissolution of some precipitates while others coarsen during the cooling period [74].

Table 0.1. Peak temperature.

Sample ID	Parameters	Peak temperature (°C)
FSW-20	Cooling (20 psi)	305
FSW-10	Cooling (10 psi)	327
FSW-0	Normal FSW	375
FSW-10A	Heating (10 A)	382
FSW-20A	Heating (20 A)	386

Moreover, the hardness profile in Figure 0.32 is asymmetrical concerning the weld centerline because the plastic flow field on the two sides of the weld center is not uniform. The piling of materials on the advancing side is more severe than that on the retreating side. Larger distorted grains and distortion energy causes strain-hardening to markedly increase, resulting in the asymmetrical microhardness distribution [75].

Figure 0.33 shows that the overall hardness tends to decrease when higher preheating is performed on the samples. The highest observed hardness values in the weld zones of FSW-10A and FSW-20A samples are 78.6 VHN and 75.1 VHN, respectively.

Looking closely at Figure 0.34, the highest microhardness reported in the weld zones is 88.4 VHN in the NZ for the FSW-20 sample. It is also be observed that the microhardness in the TMAZ is close to that in NZ as they have a very similar microstructure because they go through similar conditions during the welding process. The lowest microhardness is seen in the HAZ of the FSW-10 sample, and it is very close to that of the FSW-0 sample. Moreover, it is seen that hardness in TMAZ increased slightly in both the post cooled samples compared to the FSW-0 sample.

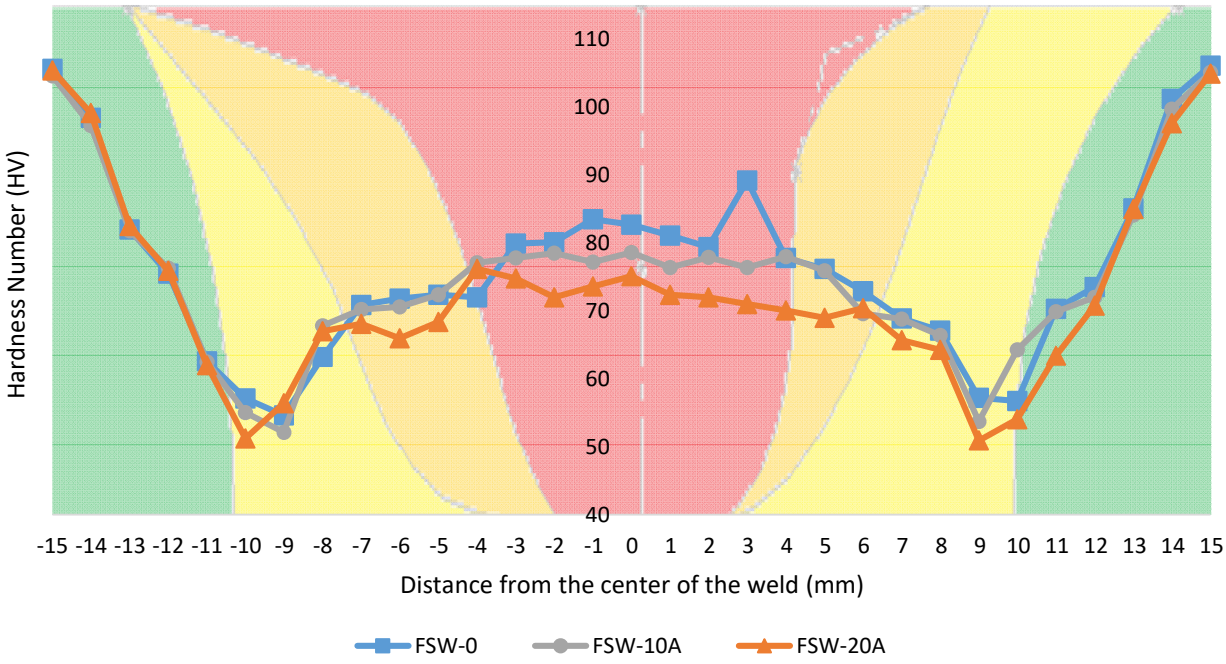

Figure 0.33. Microhardness (HV) for preheated samples (Red-WZ, orange- TMAZ, yellow-HAZ, green- PM).

From Figures 0.33 and 0.34, it is seen that a significant part of the hardness profile of post cooled samples is higher than that of the FSW-0 samples, whereas the hardness profile of the preheated samples is lower. Preheating helps in reducing the tool wear along with higher welding speeds. However, as the weld experiences higher temperatures, this results in the softening of the metal, leading to lower hardness. Also, it is seen that the HAZ is the least affected zone, almost no hardness change in preheated or post cooled samples.

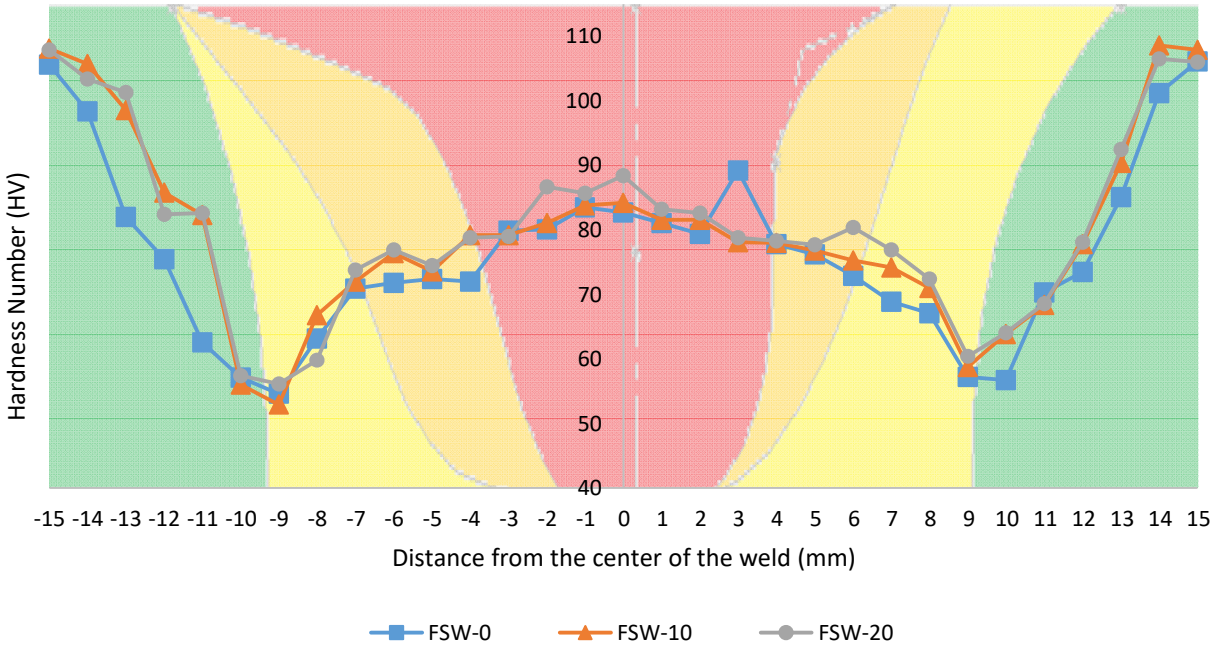

Figure 0.34. Microhardness (HV) for Postcooled samples (Red-WZ, orange- TMAZ, yellow-HAZ, green- PM).

It was noticed that the grain size did not play a significant role in determining the overall hardness profiles in various zones, with the exception of the NZ. Smaller grain size resulted in higher hardness compared to other zones for all the samples even after the dissolution of all the precipitates. Overall, the hardness profile trend is PM > NZ > TMAZ > HAZ. Hansen et al. [76] reported that in metals with high stacking fault energy, the effect of total dislocation density on the flow stress is limited, and hence it may be possible that it is not significantly affected by the grain size. Hence, it can be concluded that the grain size might not have a significant impact on the hardness. Overall, the hardness profile trend is PM > NZ > TMAZ > HAZ.

1.21 Fractography

Figures 0.35, 0.36, 0.37, 0.38, and 0.39, show fractured surfaces of the welded samples. The bright spots seen in Figure 0.35 are the impurities that get charged up when electrons are incident on them. It is seen that the mode of failure was ductile, and in most of the samples, the fracture took

place in the HAZ of the retreating side. A typical cup and cone morphology was noticed on the fractured surfaces. Based on the OM, EBSD hardness results, it can be seen that the HAZ is exposed to a higher temperature during the FWS process, which results in coarsened grains with the lowest hardness values in all the samples. There is evidence of overaged precipitate structure in the HAZ reported in the literature and based on the temperature distribution in the weld zones [72]. This also confirms that it is the weakest zone, and hence failures occur in the HAZ. Moreover, Fonda et al. [73] have reported fracture in the region of TMAZ/HAZ citing the lack of fine strengthening precipitates due to the coarsening of initial precipitates and insufficient reprecipitation during cooling.

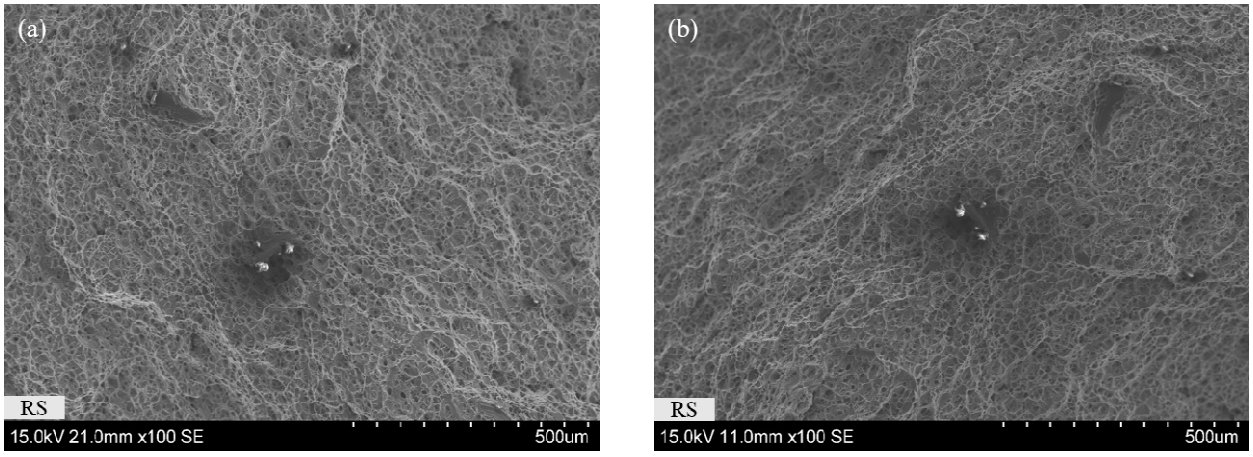

Figure 0.35. Fractured surfaces of FSW-0 sample showing failure in the HAZ of RS.

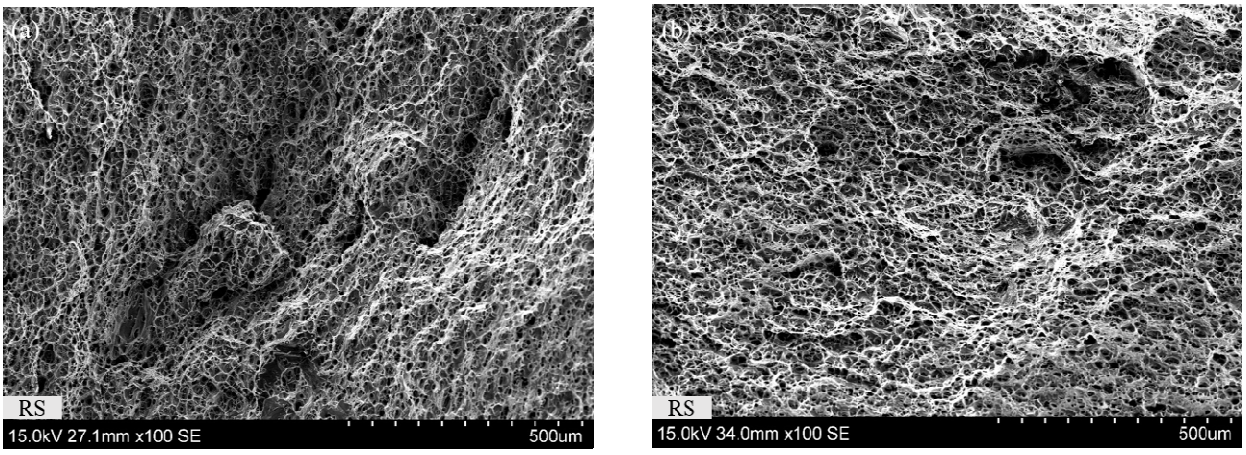

Figure 0.36. Fracture surfaces of FSW-10 sample showing failure in the HAZ of RS.

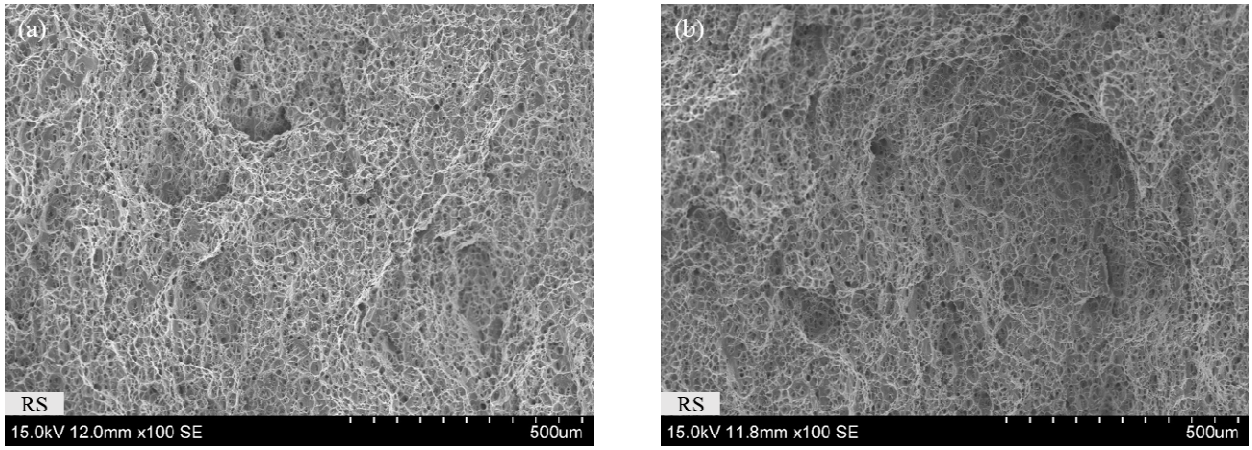

Figure 0.37. Fracture surfaces of FSW-20 sample showing failure in the HAZ of RS.

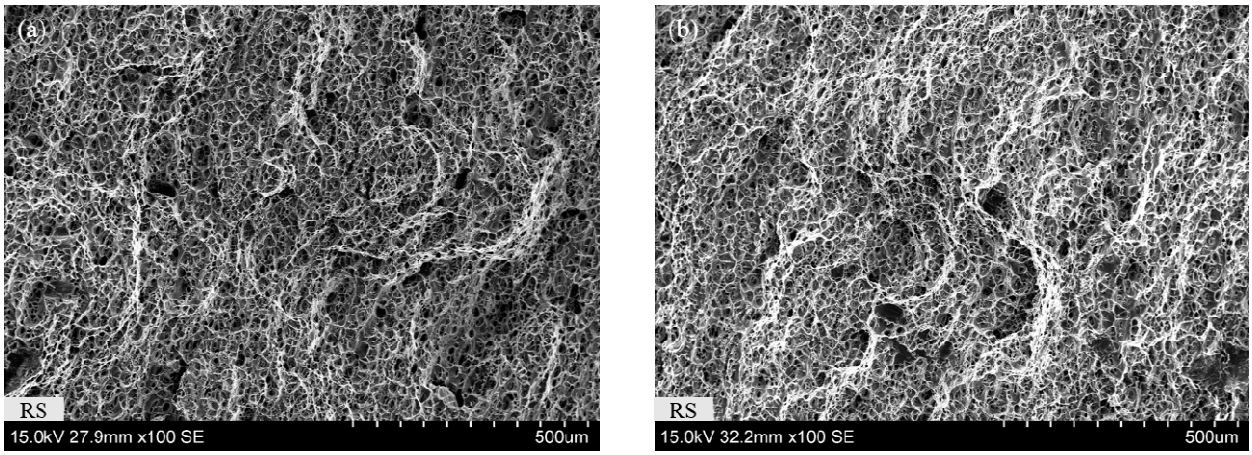

Figure 0.38. Fracture surfaces of FSW-10A sample showing failure in the HAZ of RS.

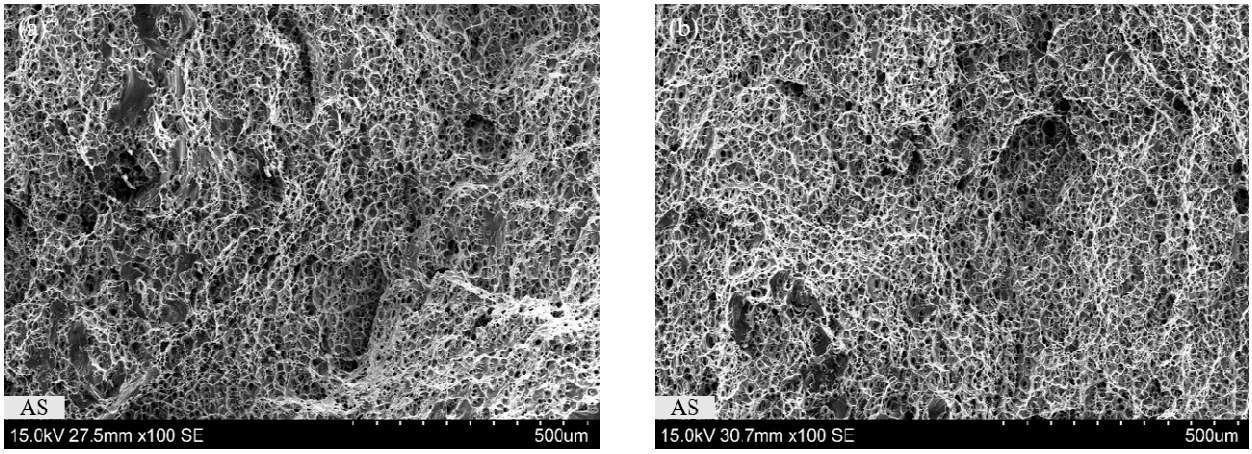

Figure 0.39. Fracture surfaces of FSW-20A sample showing failure in the HAZ of RS.

From the tensile tests conducted at ERDA (Electrical Research and Development Association), Baroda, the average tensile strength of the FSW-0 samples was measured to be 156 MPa. The average tensile strength of the preheated samples was calculated to be 154 MPa, and that of the post cooled samples was 158.5 MPa, the highest value of 165MPa for the FSW-10 samples and the lowest value of 151 MPa for the FSW-10A samples. No significant difference (less than 1%) in the average elongation was observed between the FSW-0, preheated, and post cooled samples. These results suggest that there were minor changes in the microstructure, which were not significant enough to increase the overall mechanical properties.

1.22 Overall discussion

Overall results and their effects on the mechanical properties of the welded samples under different conditions are discussed in this section. Figure 0.40 that the percentage of LAGBs is almost twice in the PM compared to that in the NZs of all the samples. Among the NZs of samples welded under different conditions, negligible change in the grain boundaries is seen. The overall trend of LAGBs in all the welded samples was observed to be TMAZ-AS > TMAZ-RS > NZ > HAZ > PM.

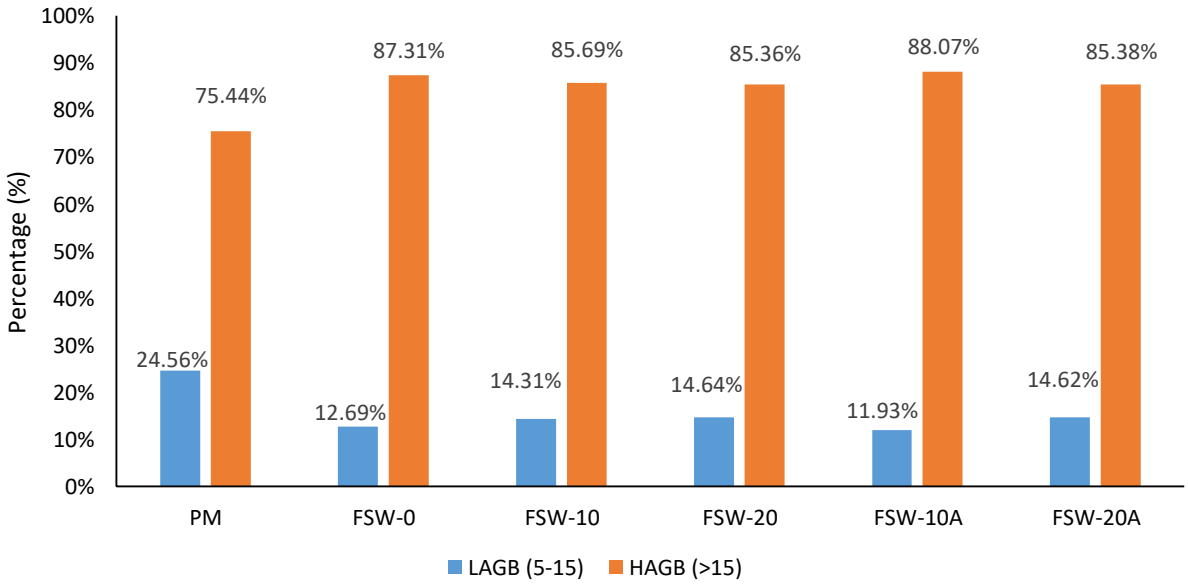

Figure 0.40. Percentage of LAGB and HAGB in the PM and at the NZs in different samples.

Figure 0.41 shows the kernel misorientation in the NZs of welded samples along with that of parent metal for reference. It is seen that the peak shift is the most in parent metal and the FSW-20 sample meaning these samples have the highest number of dislocations. On the other hand, a negligible difference is seen in the other samples.

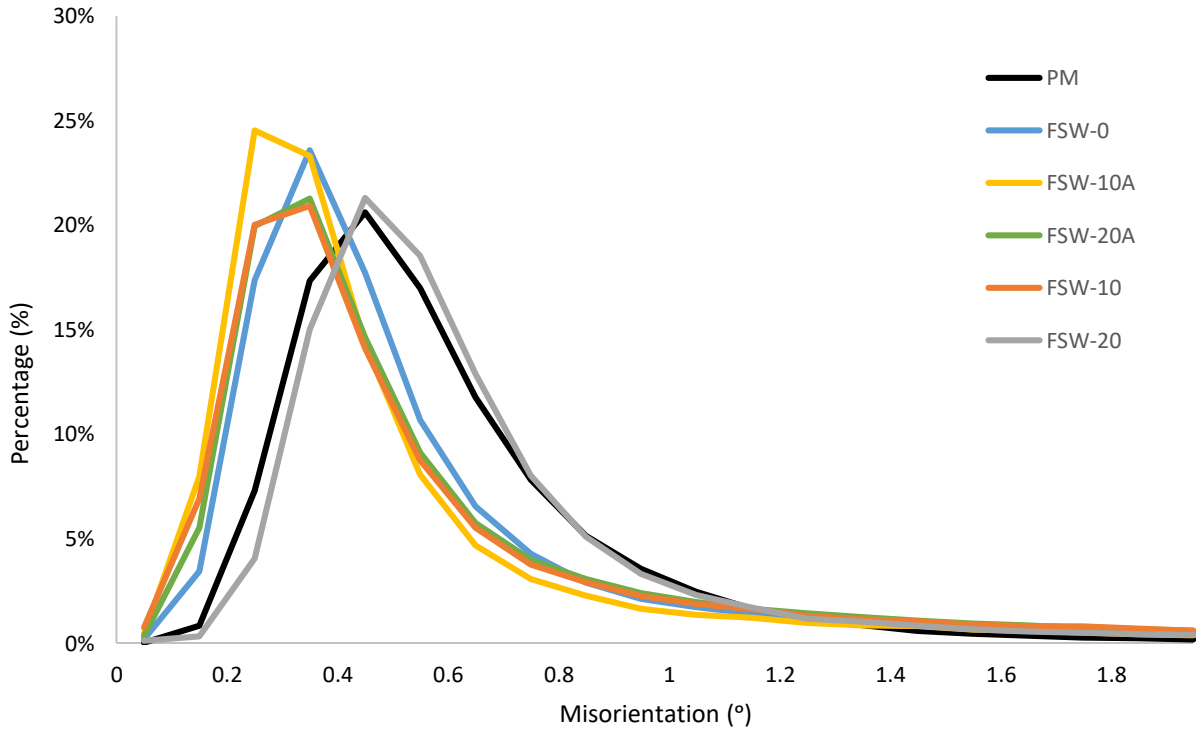

Figure 0.41. Kernel misorientation in the NZs of samples.

Figure 0.42 shows the percentage of recrystallization fraction in the NZs of samples welded under different preheating and post-cooling conditions. The effect on recrystallization of the PM and the NZ of FSW-0 samples is also mentioned as a reference. The amount of stored energy is mainly dependent on the number of dislocations. Moreover, the difference in stored energy is shown in the form of a different recrystallized fraction. Therefore, it is seen that the higher amount of substructured and deformed grains in the PM (in Figure 0.41) are the result of a higher number of dislocations in Figure 0.42. Similarly, the higher percentage of deformed grains in the FSW-20 sample is justified by a higher number of dislocations.

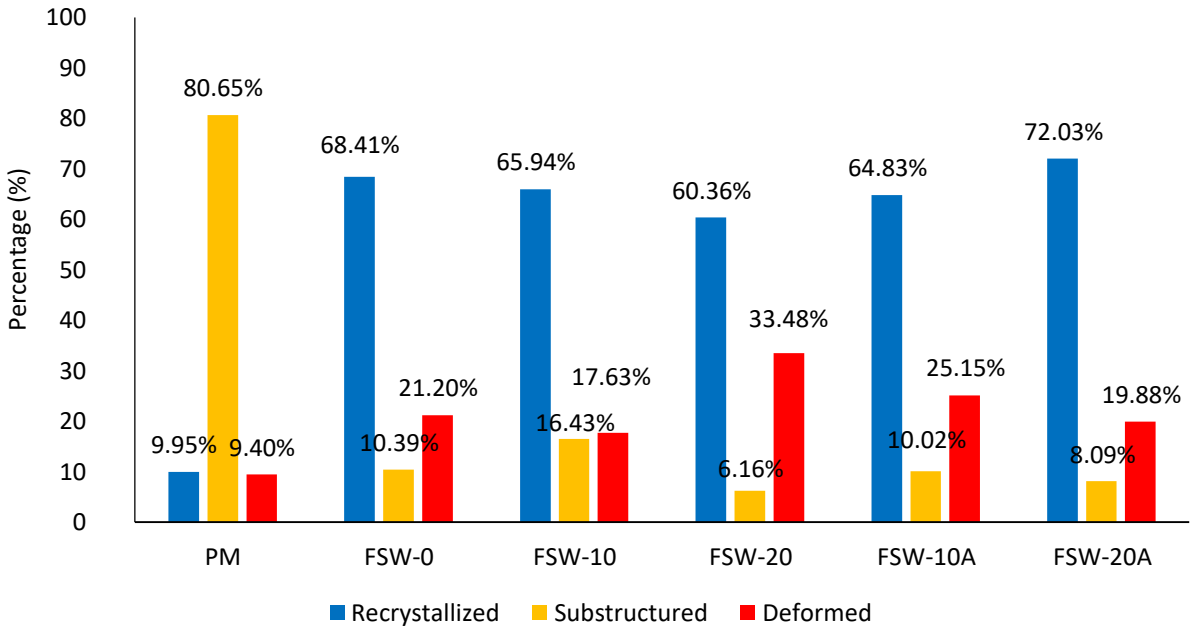

Figure 0.42. Recrystallized fraction in the NZs of samples.

The hardness profiles in all the samples with the PM hardness are shown in Figure 0.43. As mentioned before, the dislocation density and precipitate distribution are some of the main factors which contribute to the hardness. From Figures 0.41 and 0.43, it can be justified that the higher number of dislocations in the FSW-20 results in higher hardness in NZ. Moreover, the preheated samples having comparatively lower hardness values are seen to have a lower number of dislocations. However, the precipitate distribution in all the weld zones should also be taken into account to describe the overall hardness profile in various weld zones.

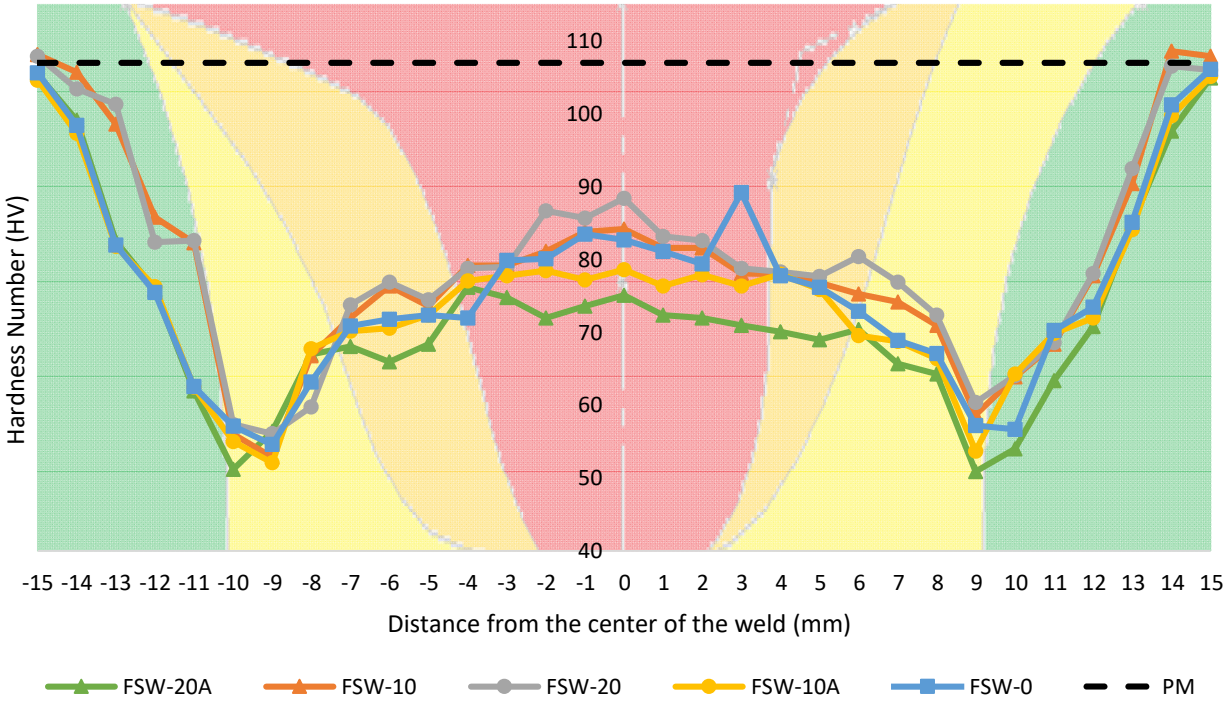

Figure 0.43. Hardness distribution in the NZs of the samples with the PM hardness as a reference.

CONCLUSIONS AND RECOMMENDATIONS

1.23 Conclusions

In the present study, the role of preheating and post-cooling on the microstructure and mechanical properties during friction stir welding was investigated. The microstructure in various weld zones was examined using various characterization techniques like optical microscopy, electron backscattered diffraction, and the fractured samples were analyzed under a scanning electron microscope. All the welds were performed, keeping the welding parameters constant while changing the intensity of preheating or post-cooling. In this manner, good quality and defect-free welds were obtained. Optical microscopy revealed that the weld coupon consists of various weld zones with different microstructural characteristics. The parent metal consists of large elongated grains with grain size around 100 µm. Highly recrystallized and equiaxed grains with a grain size of the order of 10 µm were observed in the NZ. The heat-affected zone did not undergo any deformation, but exposure to the heat cycle resulted in coarsened grains similar to the parent metal. It was also seen that the crown/top region in the NZ underwent high plastic deformation compared to the root region, and the temperature gradient resulted in slightly different microstructure in both regions. EBSD results enabled quantitative observation of the grain boundary and recrystallized fraction distribution in various weld zones. It was also seen that the dislocation density is slightly higher in the NZ of the post cooled samples compared to the preheated samples. It was concluded that precipitate distribution played a significant role whereas the grain size distribution did not affect the hardness profile significantly in the welds. Also, the HAZ was found to be the weakest zone in terms of hardness because of the coarsening of grains SEM images of the fractured surfaces revealed that most samples failed in the HAZ.and the mode of failure was ductile with cup and cone morphology. Less than a 5% change in the tensile strength was observed between the samples. Moreover, calculation of elongation from the stress-strain curves showed an insignificant difference (less than 1%) among the welded samples. Overall, it is seen that the peak temperature and the heat cycle during the welding process dictate the microstructure and mechanical properties. In contrast, plastic deformation is more responsible for proper diffusion from the advancing side to the retreating side. Preheating helps in softening the metal before welding, but it also results in 10% and 3% decrease in average hardness in the NZ of the FSW-20A and FSW-10A samples. On

the other hand, a 2% increase in average hardness in the NZ of the post cooled samples. However, the HAZ remains the weakest zone in the welds even after preheating or post-cooling.

1.24 Recommendations for future work

1. From the literature review, it can be concluded that precipitates contribute majorly to the strength, and they also get affected during the welding process because of the heating and cooling cycles, so high-resolution TEM can be used to study the types of precipitates and their distribution in the overall weldment. Also, to understand the dissolution or coarsening of precipitates at specific temperatures during the welding process, DSC can be used.
2. Texture analysis using pole figures and inverse pole figures obtained from EBSD or XRD can be useful to understand the orientation of grains in various weld zones, and texture differences might be responsible for the generation of thermal stresses within the welded zone.
3. It was established from the present research that HAZ is the weakest zone with the lowest hardness, so to improve the mechanical properties in the HAZ, certain post-weld heat treatments can be applied to the welded samples.
4. Various studies are going on to improve the overall mechanical properties of the FSW joints by cooling the welded samples using different environments like water and CO_2. Further work can be done by modifying the cooling conditions and observing their effect on the precipitates and overall mechanical properties.

REFERENCES

[1] R. N. Lumley, “Introduction to aluminium metallurgy,” in *Fundamentals of Aluminium Metallurgy: Production, Processing and Applications*, 2011, pp. 1–19.

[2] European Aluminum, “The aluminum production process.” [Online]. Available: https://www.european-aluminium.eu/about-aluminium/production-process/. [Accessed: 10-Aug-2020].

[3] “The Strength of Aluminum.” [Online]. Available: https://www.aluminum.org/strength-aluminum. [Accessed: 10-Aug-2020].

[4] “Characteristics of aluminium in fusion welding.” [Online]. Available: https://www.european-aluminium.eu/media/1517/2-aluminium-fusion-welding_2015.pdf. [Accessed: 10-Aug-2020].

[5] W. M. Thomas, E. D. Nicholas, J. C. Needham, M. G. Murch, P. Templesmith, and C. J. Dawes, “GB Patent application no. 9125978.8,” 1991.

[6] Y. J. Chao, X. Qi, and W. Tang, “Heat transfer in friction stir welding - Experimental and numerical studies,” *J. Manuf. Sci. Eng. Trans. ASME*, vol. 125, no. 1, pp. 138–145, 2003.

[7] S. Benavides, Y. Li, L. E. Murr, D. Brown, and J. C. McClure, “Low-temperature friction-stir welding of 2024 aluminum,” *Scr. Mater.*, vol. 41, no. 8, pp. 809–815, 1999.

[8] K. V Jata and S. L. Semiatin, “Continuous dynamic recrystallization during friction stir welding of high strength aluminum alloys,” *Scr. Mater.*, vol. 43, no. 8, pp. 743–749, 2000.

[9] G. Liu, L. E. Murr, C. S. Niou, J. C. McClure, and F. R. Vega, “Microstructural aspects of the friction-stir welding of 6061-T6 aluminum,” *Scr. Mater.*, vol. 37, no. 3, pp. 355–361, 1997.

[10] C. G. Rhodes, M. W. Mahoney, W. H. Bingel, R. A. Spurling, and C. C. Bampton, “Effects of friction stir welding on microstructure of 7075 aluminum,” 1997.

[11] K. J. Colligan, “The friction stir welding process: An overview,” in *Friction Stir Welding: From Basics to Applications*, Elsevier, 2009, pp. 15–41.

[12] “Friction Stir Welding - TWI.” [Online]. Available: https://www.twi-global.com/technical-knowledge/job-knowledge/friction-stir-welding-147. [Accessed: 10-Aug-2020].

[13] R. S. Mishra and Z. Y. Ma, “Friction stir welding and processing,” *Mater. Sci. Eng. R Reports*, vol. 50, no. 1–2, Aug. 2005.

[14] “Materials Weldable by Friction Stir - TWI.” [Online]. Available: https://www.twi-global.com/what-we-do/research-and-technology/technologies/welding-joining-and-cutting/friction-welding/friction-stir-welding/materials-weldable-by-friction-stir. [Accessed: 10-Aug-2020].

[15] “NASA Technical Reports Server (NTRS).” [Online]. Available: https://ntrs.nasa.gov/citations/20150009520. [Accessed: 10-Aug-2020].

[16] “Friction Stir Welding of Airframe Structures - TWI.” [Online]. Available: https://www.twi-global.com/who-we-are/who-we-work-with/industry-sectors/aerospace/joining-of-airframe-structures/friction-stir-welding-of-airframe-structures. [Accessed: 10-Aug-2020].

[17] “Friction Stir Welding to Produce Aluminium Components/Panels - TWI.” [Online]. Available: https://www.twi-global.com/technical-knowledge/published-papers/nz-fabricators-begin-to-use-friction-stir-welding-to-produce-aluminium-components-and-panels-august-2006. [Accessed: 10-Aug-2020].

[18] “Friction Stir Welding in Series Production - TWI.” [Online]. Available: https://www.twi-global.com/technical-knowledge/published-papers/friction-stir-welding-in-series-production-october-2004. [Accessed: 10-Aug-2020].

[19] J. C. Basset and S. S. ; Birley, “Friction Stir Welding of Aluminium Armour,” in *2nd International Symposium on Friction Stir Welding*, 2000, vol. 20, no. 2.

[20] K. J. Colligan, J. J. Fisher, J. E. Gover, and J. R. Pickens, “Friction stir welding in the AAAV,” *Adv. Mater. Process.*, vol. 160, no. 9, pp. 39–41, 2002.

[21] G. Campbell and T. Stotler, “Friction stir welding of armor grade aluminum plate,” *Weld. J.*, vol. 78, no. 12, pp. 45–47, 1999.

[22] K. L. Russell, Alan M; Lee, “Al, Ga, In, and Tl,” in *Structure-Property Relations in Nonferrous Metals*, Hoboken, NJ, USA: John Wiley & Sons, Inc., 2005, pp. 358–391.

[23] J. R. Kissell and R. L. Ferry, “Aluminum Structures: A Guide to Their Specifications and Design. 2002.” New York: John Wiley & Sons, Inc.

[24] W. D. Callister and D. G. Rethwisch, “Applications and Processing of Metal Alloys,” in

Materials Science and Engineering An Introduction, 9th ed., D. Sayre, Ed. Hoboken: Wiley, 2014, pp. 408–466.

[25] "Weldability of Materials - Aluminium Alloys - TWI." [Online]. Available: https://www.twi-global.com/technical-knowledge/job-knowledge/weldability-of-materials-aluminium-alloys-021. [Accessed: 11-Aug-2020].

[26] V. Fahimpour, S. K. Sadrnezhaad, and F. Karimzadeh, "Corrosion behavior of aluminum 6061 alloy joined by friction stir welding and gas tungsten arc welding methods," *Mater. Des.*, vol. 39, pp. 329–333, 2012.

[27] S. Malarvizhi and V. Balasubramanian, "Effect of welding processes on AA2219 aluminium alloy joint properties," *Trans. Nonferrous Met. Soc. China (English Ed.*, vol. 21, no. 5, pp. 962–973, 2011.

[28] A. K. Lakshminarayanan, V. Balasubramanian, and K. Elangovan, "Effect of welding processes on tensile properties of AA6061 aluminium alloy joints," *Int. J. Adv. Manuf. Technol.*, vol. 40, no. 3–4, pp. 286–296, 2009.

[29] D. A. Price *et al.*, "Distortion control in welding by mechanical tensioning," *Sci. Technol. Weld. Join.*, vol. 12, no. 7, pp. 620–633, 2007.

[30] R. Nandan, T. DebRoy, and H. K. D. H. Bhadeshia, "Recent advances in friction-stir welding - Process, weldment structure and properties," *Prog. Mater. Sci.*, vol. 53, no. 6, pp. 980–1023, 2008.

[31] Y. H. Zhao, S. B. Lin, F. X. Qu, and L. Wu, "Influence of pin geometry on material flow in friction stir welding process," *Mater. Sci. Technol.*, vol. 22, no. 1, pp. 45–50, 2006.

[32] W. M. Thomas, K. I. Johnson, and C. S. Wiesner, "Friction stir welding-recent developments," in *Materials Science Forum*, 2003, vol. 426, no. 7, pp. 229–236.

[33] W. M. Thomas, K. I. Johnson, and C. S. Wiesner, "Friction stir welding-recent developments in tool and process technologies," *Adv. Eng. Mater.*, vol. 5, no. 7, pp. 485–490, 2003.

[34] W. M. Thomas, D. G. Staines, K. I. Johnson, and P. Evans, "Com-stir–compound motion for friction stir welding and machining," *Adv Eng Mater*, vol. 5, pp. 273–274, 2003.

[35] W. M. Thomas, E. D. Nicholas, J. C. Needham, M. G. Murch, P. Temple-Smith, and C. J. Dawes, "Improvements relating to friction welding," *Eur. Pat. Specif. 0*, vol. 615, no. 480,

p. B1, 1992.

[36] W. M. Thomas, E. D. Nicholas, J. C. Needham, M. G. Murch, P. Templesmith, and C. J. Dawes, “Improvements relating to friction welding. International Patent Application,” PCT/GB92/02203 (Patent) December, 1991.

[37] F. C. Liu and Z. Y. Ma, “Influence of tool dimension and welding parameters on microstructure and mechanical properties of friction-stir-welded 6061-T651 aluminum alloy,” *Metall. Mater. Trans. A Phys. Metall. Mater. Sci.*, vol. 39, no. 10, pp. 2378–2388, 2008.

[38] J. Yan, M. A. Sutton, and A. P. Reynolds, “Process-structure-property relationships for nugget and heat affected zone regions of AA2524-T351 friction stir welds,” *Sci. Technol. Weld. Join.*, vol. 10, no. 6, pp. 725–736, 2005.

[39] Y. J. Kwon, I. Shigematsu, and N. Saito, “Mechanical properties of fine-grained aluminum alloy produced by friction stir process,” *Scr. Mater.*, vol. 49, no. 8, pp. 785–789, 2003.

[40] W. Tang, X. Guo, J. C. McClure, L. E. Murr, and A. Nunes, “Heat input and temperature distribution in friction stir welding,” *J. Mater. Process. Manuf. Sci.*, vol. 7, no. 2, pp. 163–172, 1998.

[41] A. Arici and S. Selale, “Effects of tool tilt angle on tensile strength and fracture locations of friction stir welding of polyethylene,” *Sci. Technol. Weld. Join.*, vol. 12, no. 6, pp. 536–539, Aug. 2007.

[42] K. R. Seighalani, M. K. B. Givi, A. M. Nasiri, and P. Bahemmat, “Investigations on the effects of the tool material, geometry, and tilt angle on friction stir welding of pure titanium,” *J. Mater. Eng. Perform.*, vol. 19, no. 7, pp. 955–962, 2010.

[43] Y. S. Sato, H. Kokawa, M. Enomoto, S. Jogan, and T. Hashimoto, “Precipitation sequence in friction stir weld of 6063 aluminum during aging,” *Metall. Mater. Trans. A Phys. Metall. Mater. Sci.*, vol. 30, no. 12, pp. 3125–3130, 1999.

[44] J. Q. Su, T. W. Nelson, R. Mishra, and M. Mahoney, “Microstructural investigation of friction stir welded 7050-T651 aluminium,” *Acta Mater.*, vol. 51, no. 3, pp. 713–729, 2003.

[45] A. P. Reynolds, W. D. Lockwood, and T. U. Seidel, “Processing-property correlation in friction stir welds,” in *Materials science forum*, 2000, vol. 331, pp. 1719–1724.

[46] H. Kafali and N. Ay, “The effect of post heat treatment on the fatigue behavior of riction

stir welded aluminum 6013 alloy for use in aerospace structures," *J. Int. Sci. Publ. Mater. Methods Technol.*, vol. 8, pp. 405–417, 2012.

[47] K. N. Krishnan, "The effect of post weld heat treatment on the properties of 6061 friction stir welded joints," *J. Mater. Sci.*, vol. 37, no. 3, pp. 473–480, 2002.

[48] H. Aydin, A. Bayram, and I. Durgun, "The effect of post-weld heat treatment on the mechanical properties of 2024-T4 friction stir-welded joints," *Mater. Des.*, vol. 31, no. 5, pp. 2568–2577, 2010.

[49] P. Patel, H. Rana, V. Badheka, V. Patel, and W. Li, "Effect of active heating and cooling on microstructure and mechanical properties of friction stir–welded dissimilar aluminium alloy and titanium butt joints," *Weld. World*, vol. 64, no. 2, pp. 365–378, 2020.

[50] D. Venkateswarulu, M. Cheepu, D. Krishnaja, and S. Muthukumaran, "Influence of Water Cooling and Post-Weld Ageing on Mechanical and Microstructural Properties of the Friction-Stir Welded 6061 Aluminium Alloy Joints," *Appl. Mech. Mater.*, vol. 877, no. December 2017, pp. 163–176, 2018.

[51] H. S. Bang, H. S. Bang, G. H. Jeon, I. H. Oh, and C. S. Ro, "Gas tungsten arc welding assisted hybrid friction stir welding of dissimilar materials Al6061-T6 aluminum alloy and STS304 stainless steel," *Mater. Des.*, vol. 37, pp. 48–55, 2012.

[52] T. Tanaka, T. Morishige, and T. Hirata, "Comprehensive analysis of joint strength for dissimilar friction stir welds of mild steel to aluminum alloys," *Scr. Mater.*, vol. 61, no. 7, pp. 756–759, 2009.

[53] M. Merklein and A. Giera, "Laser assisted Friction Stir Welding of drawable steel-aluminium tailored hybrids," *Int. J. Mater. Form.*, 2008.

[54] R. S. Funderburk, "Fundamentals of Preheat," vol. XIV, no. 2, pp. 1–2, 1997.

[55] K. P. Mehta and V. J. Badheka, "Hybrid approaches of assisted heating and cooling for friction stir welding of copper to aluminum joints," *J. Mater. Process. Technol.*, vol. 239, pp. 336–345, 2017.

[56] G. M. Reddy, P. Mastanaiah, K. S. Prasad, and T. Mohandas, "Microstructure and mechanical property correlations in AA 6061 aluminium alloy friction stir welds," *Trans. Indian Inst. Met.*, vol. 62, no. 1, pp. 49–58, 2009.

[57] K. Elangovan and V. Balasubramanian, "Influences of post-weld heat treatment on tensile

properties of friction stir-welded AA6061 aluminum alloy joints," *Mater. Charact.*, vol. 59, no. 9, pp. 1168–1177, 2008.

[58] R. B. C. Cayless, "Alloy and Temper Designation Systems for Aluminum and Aluminum Alloys," *ASM Handbook, Vol. 2 Prop. Sel. Nonferrous Alloy. Spec. Mater.*, vol. 2, pp. 15–28, 1990.

[59] eFunda Inc, "Tool Steel - AISI T2." [Online]. Available: http://www.efunda.com/glossary/materials/alloys/materials--alloys--steel--tool_steel--aisi_t2.cfm. [Accessed: 10-Aug-2020].

[60] R. S. Coelho, A. Kostka, J. F. Dos Santos, and A. R. Pyzalla, "EBSD technique visualization of material flow in aluminum to steel friction-stir dissimilar welding," *Adv. Eng. Mater.*, vol. 10, no. 12, pp. 1127–1133, Dec. 2008.

[61] C. Herrera, D. Ponge, and D. Raabe, "Design of a novel Mn-based 1 GPa duplex stainless TRIP steel with 60% ductility by a reduction of austenite stability," *Acta Mater.*, vol. 59, no. 11, pp. 4653–4664, 2011.

[62] R. Badji, T. Chauveau, and B. Bacroix, "Texture, misorientation and mechanical anisotropy in a deformed dual phase stainless steel weld joint," *Mater. Sci. Eng. A*, vol. 575, pp. 94–103, 2013.

[63] W. B. Lee, Y. M. Yeon, and S. B. Jung, "Mechanical properties related to microstructural variation of 6061 Al alloy joints by friction stir welding," *Mater. Trans.*, vol. 45, no. 5, pp. 1700–1705, 2004.

[64] P. Gerber, J. Tarasiuk, T. Chauveau, and B. Bacroix, "A quantitative analysis of the evolution of texture and stored energy during annealing of cold rolled copper," *Acta Mater.*, vol. 51, no. 20, pp. 6359–6371, 2003.

[65] F. J. Humphreys and M. Hatherly, "Recrystallization of Single-Phase Alloys," in *Recrystallization and Related Annealing Phenomena*, 2nd ed., Elsevier, 2004, pp. 215–267.

[66] N. P. Gurao, A. O. Adesola, A. G. Odeshi, and J. A. Szpunar, "On the evolution of heterogeneous microstructure and microtexture in impacted aluminum-lithium alloy," *J. Alloys Compd.*, vol. 578, pp. 183–187, 2013.

[67] Y. S. Sato, F. Yamashita, Y. Sugiura, S. H. C. Park, and H. Kokawa, "FIB-assisted TEM study of an oxide array in the root of a friction stir welded aluminium alloy," *Scr. Mater.*,

vol. 50, no. 3, pp. 365–369, 2004.

[68] O. Hisanori, A. Kinya, S. Masahiko, E. Masakuni, and I. Kenji, “Behavior of oxide during friction stir welding of aluminum alloy and its influence on mechanical properties,” *Q. J. Japan Weld. Soc.*, vol. 19, no. 3, pp. 446–456, 2001.

[69] C. Zhou, X. Yang, and G. Luan, “Effect of oxide array on the fatigue property of friction stir welds,” *Scr. Mater.*, vol. 54, no. 8, pp. 1515–1520, 2006.

[70] M. W. Mahoney, C. G. Rhodes, J. G. Flintoff, R. A. Spurling, and W. H. Bingel, “Properties of friction-stir-welded 7075 T651 aluminum,” *Metall. Mater. Trans. A Phys. Metall. Mater. Sci.*, vol. 29, no. 7, pp. 1955–1964, 1998.

[71] J. A. Schneider and A. C. Nunes, “Characterization of plastic flow and resulting microtextures in a friction stir weld,” *Metall. Mater. Trans. B Process Metall. Mater. Process. Sci.*, vol. 35, no. 4, pp. 777–783, 2004.

[72] B. Heinz and B. Skrotzki, “Characterization of a friction-stir-welded aluminum alloy 6013,” *Metall. Mater. Trans. B Process Metall. Mater. Process. Sci.*, vol. 33, no. 3, pp. 489–498, 2002.

[73] R. W. Fonda and J. F. Bingert, “Microstructural evolution in the heat-affected zone of a friction stir weld,” *Metall. Mater. Trans. A Phys. Metall. Mater. Sci.*, vol. 35 A, no. 5, pp. 1487–1499, 2004.

[74] Y. S. Sato, H. Kokawa, M. Enomoto, and S. Jogan, “Microstructural evolution of 6063 aluminum during friction-stir welding,” *Metall. Mater. Trans. A Phys. Metall. Mater. Sci.*, vol. 30, no. 9, pp. 2429–2437, 1999.

[75] W. Xu, J. Liu, G. Luan, and C. Dong, “Temperature evolution, microstructure and mechanical properties of friction stir welded thick 2219-O aluminum alloy joints,” *Mater. Des.*, vol. 30, no. 6, pp. 1886–1893, 2009.

[76] N. Hansen, X. Huang, and G. Winther, “Effect of grain boundaries and grain orientation on structure and properties,” *Metall. Mater. Trans. A Phys. Metall. Mater. Sci.*, vol. 42, no. 3, pp. 613–625, 2011.